Chemical Engineering Journal 548 (2026) 181521

Contents lists available at ScienceDirect

Chemical Engineering Journal

journal homepage: www.elsevier.com/locate/cej

Experimental study of microalgae chemical looping gasification with ilmenite, LD slag and iron sand in a 1.5 kW_{th} unit

Hantao Lu [a,b], Daofeng Mei [a,c,*], Francisco García-Labiano [a], Juan Ignacio Ruiz Irizar [a], Maria Teresa Izquierdo [a], Alberto Abad [a], Guangsuo Yu [b]

[a] Instituto de Carboquímica (ICB-CSIC), Miguel Luesma Castán 4, Zaragoza 50018, Spain
[b] Institute of Clean Coal Technology, East China University of Science and Technology, Shanghai, 200237, PR China
[c] The Aragonese Foundation for Research & Development (ARAID), Avenida de Ranillas 1D, 50018, Zaragoza, Spain

ARTICLE INFO

Keywords:
Chemical looping gasification
Syngas
Microalgae
Oxygen carrier
Characterization
Tar yield

ABSTRACT

Chemical looping gasification (CLG) enables production of nitrogen-free syngas without need of air separation, thus offering a promising route for efficient biomass conversion. Microalgae, as a third-generation biofuel feedstock, present advantages in sustainability but pose challenges due to their high ash content. In this study, ilmenite, LD slag (a steelmaking byproduct from the Linz-Donawitz process), and iron sand were evaluated as oxygen carriers for microalgae CLG in a 1.5 kW_{th} unit. The experiments were performed in various operating conditions and lasted 20–25 h with each oxygen carrier. Effects of key operational parameters including oxygen-to-biomass ratio (λ, 0.13–0.51), fuel reactor (FR) temperature (860–920 °C), and gasifying agent composition (H_2O/CO_2 ratio, 100/0, 50/50 and 0/100) were investigated. The CLG performance was assessed with product gas composition, biomass conversion, carbon emitted from AR, syngas yield, cold gas efficiency, and tar formation that are essential for gasification processes. Oxygen carrier samples before and after the experimental campaigns were characterized with ICP-AES, XRD and SEM-EDX techniques to study changes in the physico-chemical properties of the materials and their interactions with ash components of the microalgae. A TGA analysis was done to study the reactivity change of the materials during the campaign. Among the three materials, the LD slag exhibited the most promising overall performance. With this oxygen carrier, the syngas reached 1.5 Nm^3/kg microalgae and the tar yield was suppressed to 0.5 g/kg. The outstanding performance with LD slag is deemed as a result of rich Ca content in the material, as calcium is a classical catalyst promoting gasification.

1. Introduction

The growing environmental and energy challenges associated with fossil-fuel consumption encourage the search of sustainable and low-carbon energy conversion systems [1]. Biomass gasification is a promising thermochemical route for converting renewable biomass into syngas for various applications [2,3]. The conventional gasification suffers from limited efficiency and the lack of efficient CO_2 capture [4]. On the contrary, biomass chemical looping gasification (BCLG) produces syngas in an unmixed configuration [5], where syngas is not mixed with air [6]. In this way, the syngas stream is free from dilution by air or N_2, which facilitates downstream gas cleaning and CO_2 capture [7,8].

As illustrated in Fig. 1, the BCLG system consists of two interconnected fluidized-bed reactors: an air reactor (AR) and a fuel reactor (FR). A circulating oxygen carrier (OC)—normally a metal oxide (Me_xO_y)—is oxidized in the AR and then transported to the FR, where it provides lattice oxygen and sensible heat for the biomass conversion. In the FR, the biomass undergoes devolatilization, and the resulting volatiles and char react with steam or CO_2 and the OC to generate syngas that is rich in H_2 and CO. Meanwhile, the OC is reduced to Me_xO_{y-1}. The reduced OC particles are then transferred to the AR to oxidize back to its oxidization state, completing the loop. Several key reactions occur in the FR, including devolatilization, char gasification and water-gas reactions, and partial oxidation mediated by the OC. The present of OC also promotes tar cracking if the OC is catalytic, and this lowers issues caused by tar and contributes to a higher syngas quality. Auto-thermal operation can be also achieved in suitable conditions, as the heat from exothermic oxidation in the AR can be transferred to the FR through circulation of the hot OC particles. Because of the special reactor configurations, the

* Corresponding author at: Instituto de Carboquímica (ICB-CSIC), Miguel Luesma Castán 4, Zaragoza, 50018, Spain.
E-mail address: dmei@icb.csic.es (D. Mei).

https://doi.org/10.1016/j.cej.2026.181521
Received 23 June 2026; Received in revised form 8 August 2026; Accepted 2 September 2026
Available online 3 September 2026
1385-8947/© 2026 The Authors. Published by Elsevier B.V. This is an open access article under the CC BY license (http://creativecommons.org/licenses/by/4.0/).

Nomenclature and units

AR	Air Reactor
CLG	Chemical looping gasification
FR	Fuel Reactor
ICP-AES	Inductively Coupled Plasma Atomic Emission Spectroscopy
OC	Oxygen carrier
SEM-EDX	Scanning Electron Microscopy coupled with Energy Dispersive X-ray Spectroscopy
TGA	Thermogravimetric analyzer
XRD	X-ray diffraction
$C_{AR,emit}$	Carbon emitted from AR [%]
$F_{C,AR,out}$	Carbon flow out of AR [mol/s]
$F_{C,FR,out}$	Carbon flow out of FR [mol/s]
$F_{C,b}$	Carbon flow to the FR [mol/s]
F_b	Biomass flow to the FR [kg/s]
$F_{g,FR,out}$	Molar gas flowrate obtained from FR outlet [mol/s]
F_{NOx}	Molar flow of NOx gases (NO, N_2O and NO_2) at FR outlet [mol/s]
$F_{Nfuel,in}$	Molar flow of nitrogen in the microalgae entering the system [mol/s]
$F_{O2,AR,in}$	Oxygen flow to the AR [mol/s]
$\Delta H_{comb,i}$	Low heating value of gas i (i = CO, H_2 and CH_4) [kJ/mol]
LHV_b	Low heating value of biomass [kJ/kg]
m	Instantaneous mass of the oxygen carrier sample in the TGA tests [g]
m_o	Mass of completely oxidized oxygen carrier sample in the TGA tests [g]
m_r	Mass of completely reduced oxygen carrier sample in the TGA tests [g]
p_{ref}	reference partial pressure of gas for the calculation of normalized reactivity [atm]
p_{TGA}	partial pressure of the reducing gas in the TGA [atm]
R_{OC}	Oxygen transport capacity [wt%]
x_i	Mass fraction of component i in pretreated microalgae [%]
X_b	Solid fuel conversion [%]
X_{fn}	Conversion of microalgae nitrogen [%]
$X_{o,OC}$	oxidation degree of oxygen carrier in the TGA tests
$X_{r,OC}$	reduction degree of oxygen carrier in the TGA tests
Y	Syngas yield [Nm^3/kg of dry microalgae]
$(dX_{r,OC}/dt)_{norm}$	normalized reactivity of the oxygen carrier sample based on TGA data [%/min]
λ	Oxygen-to-biomass ratio
χ_{dnf}	Dry-and-nitrogen free gas concentration [%]
χ_i	Molar concentration of gas i (CH4, CO, CO_2, H_2) leaving the FR [%]
η_g	Cold gas efficiency, CGE [%]
Ω_b	Stoichiometric oxygen for full biomass combustion [mol O/kg microalgae]

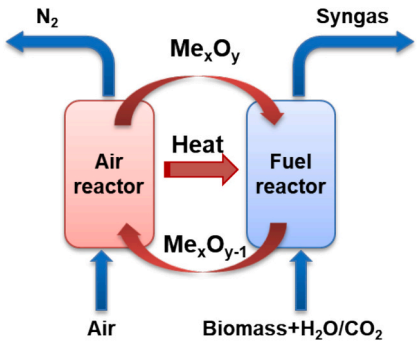


Fig. 1. Illustration of the BCLG process.

BCLG offers several other advantages, such as a lower risk of corrosion to heat-exchangers that are supposed to put at downstream of the AR reactor. This is due to the physical separation of fuel conversion and heat-exchange zones [9,10]. Because biomass is used as the feedstock, BCLG enables carbon-neutral and this becomes carbon-negative when the carbon capture is implemented, making it a promising pathway for sustainable biofuels and bio-based chemicals production [11].

Microalgae have gained attentions as a precursor for third-generation biofuels [12] due to their rapid growth [13], low production cost, and adaptability to cultivation in freshwater, wastewater, and marine environments [14]. Unlike conventional lignocellulosic biomass, microalgae do not compete with food chain and have high CO_2 fixation capacity [12]. Previous works include hydrogen production via supercritical water gasification [15,16] accounting for effect of catalysts, and the gasification is clearly enhanced by catalysis. Sun et al. [17] optimized microalgae gasification to improve process performance and sustainability. However, microalgae also present unique challenges compared with woody or herbaceous biomass. Their high ash content and inorganic constituents may cause problematic operational issues, such as heat-exchanger corrosions [18,19]. BCLG can handle this problem well, which makes microalgae particularly attractive for integration with BCLG to produce high-quality syngas. However, research on microalgae in BCLG process is scarce, and only several (3–4) publications are available and most of these studies were conducted in small-scale or fixed-bed systems that do not fully capture the real process in real CLG reacting conditions [20–22], and little information can be extracted for the technology's scale-up. Thus, study of microalgae-CLG with continuous pilots is of highly interest and is an important step for scale-up of the BCLG technology.

Inexpensive materials are desired for the BCLG process, because the ash removal from the gasifier may cause significant losses of OC [23]. Fe-based materials, including naturally abundant minerals such as ilmenite, LD slag and iron sand are low-cost and widely available OCs, and are suitable for integration into BCLG systems [23,24]. Their global abundance, established supply chains, and prior experience for use in chemical looping applications make them attractive for BCLG process. Ilmenite [25], a naturally occurring Fe—Ti oxide, is well known for its stable redox properties, mechanical durability, and consistent reactivity in fluidized-bed reactors. Its successful operation in bench and pilot-scale CLG units has established it as a benchmark material for evaluating OC performance [26,27]. LD slag [28], produced as a by-product of steelmaking in the Linz-Donawitz process, contains iron- and calcium-rich mineral phases that enable a favorable reactivity for gasification and reforming reactions. Recent tests have shown that LD slag can generate high-quality syngas with reduced tar formation [29]. Iron sand [30], another iron-rich industrial by-product, also exhibits suitable oxygen-transfer capacity and stable behavior during looping cycles, while offering excellent cost and availability advantages. Both LD slag and iron sand have shown promising results in pilot reactors [31,32]. Ilmenite, LD slag, and iron sand have been studied in CLG with 1st and 2nd generation biomasses, such as woody residues, agricultural straw, and dedicated energy crops (e.g., miscanthus) [31].

While ilmenite, LD slag, and iron sand oxygen carriers have shown promise with 1st and 2nd generation biomasses, their behavior with microalgae for 3rd generation biofuel production remains largely unexplored. In particular, there is still a lack of systematic evaluation of their overall gasification performance, including syngas yield, carbon conversion, and redox stability particularly in continuous BCLG plant.

Such knowledge is essential for identifying degradation pathways and establishing selection criteria for durable materials. Therefore, the present study aims to comparatively assess ilmenite, LD slag, and iron sand in a 1.5 kW_{th} BCLG system using microalgae as feedstock, and thus to select a most suitable OC from these candidates. Through comprehensive characterization and reaction analysis, this work seeks to identify a most suitable OC for microalgae-based BCLG and to provide new insights into OC evolution under the condition with ash-rich fuels.

The objective of this study is to compare and evaluate the ilmenite, LD slag and iron sand and select a most suitable OC for continuous microalgae CLG operation. While previous works are mostly done in small-scale and fixed-bed with microalgae, this work brings microalgae-CLG to a higher level with continuous pilot, thereby, providing relevant and useful information that support future scale-up of this technology. The influence of key operating variables, including the oxygen-to-biomass ratio, the FR temperature, and the gasifying agent (steam, CO_2 or their mixture), was independently assessed. Particular attention was paid to the evolution of syngas composition, gasification efficiency, and tar formation under steady-state conditions. In parallel, OC samples collected before and after operation were extensively characterized to examine structural changes, phase transformations, and reaction-induced degradation associated with the high alkali and alkaline earth metallic (AAEM) species content of microalgae. To the authors' knowledge, this is the first systematic study to comparatively evaluate low-cost oxygen carriers for continuous microalgae CLG in a pilot-scale unit while simultaneously considering both gasification performance and material evolution. By combining process performance evaluation with material characterization, this work establishes selection criteria for OCs in microalgae CLG and provides insights into the interactions between OC and gasification performance, offering guidance for future larger scale applications.

2. Experimental

2.1. OCs and microalgae

Ilmenite, LD slag and iron sand are used in the current work. The ilmenite is a titanium-iron natural ore originating from Norway, and the LD slag and iron sand are industrial by-products from steelmaking through Linz-Donawitz process and copper smelting processes, respectively. The LD slag and iron sand have shown good CLG performance with microalgae in our previous experiments but with a batch reactor [33], while the ilmenite is also considered as a candidate and a benchmark material for comparison. All the materials were heat-treated at 950 °C for 6 h in air atmosphere to improve their thermal and physical stability before use in the CLG process. The pretreated samples were sieved to particles with a size of 100–300 μm for use in the 1.5 kW_{th} unit, and for the ilmenite, the material has been used previously with waste wood before experiments with microalgae to reach an activated state of the material. The ilmenite activation was to reach a stable reactivity while keeping the material clean from contamination of ash alkalis before use with microalgae. So, the waste wood which contains little ash content was used for the activation. Different to ilmenite, the LD slag and iron sand have relatively stable activities, so they were put into the reactor in fresh states. All these ensure a same start point for comparison of the three oxygen carriers: clean and activated (or stable). Table 1 displays the composition, active redox phases and oxygen transport capacity of the particles. The oxygen transport capacity (R_{OC}) is an important parameter in chemical looping process because this parameter indicates the fraction of available oxygen in the materials. The main phases and active redox pairs of these OCs are also shown in the table, and these were determined through X-ray diffraction (XRD) characterization and thermogravimetric analyzer (TGA) experiments [34].

Table 1
Main composition of the three OCs.

	R_{OC} (at 950 °C)	Main XRD phase for raw materials	Main active redox system (Me_xO_y-Me_xO_{y-1})
Ilmenite	3.7%	Fe_2TiO_5, Fe_2O_3, TiO_2	Fe_2TiO_5/$FeTiO_3$ - Fe_2O_3/Fe_3O_4
LD slag	1.2%	CaO, Ca_2SiO_4, $Ca_2Fe_2O_5$	$Ca_2Fe_2O_5$ - $CaFe_3O_5$
Iron sand	1.3%	Fe_2O_3, Fe_3O_4, Fe_2SiO_4	Fe_2O_3 - Fe_3O_4

The raw microalgae (*Spirulina*) feedstock was purchased from 4BlueTech in Barcelona and received in form of fine powders. The powders were granulated, dried, sieved and heat-treated before use in the experiments. In the granulation, only deionized water was used as the binder. The granulates were then dried overnight at room temperature and sieved to particles with size of 0.2–0.8 mm, and at last these particles were subject to a first pretreatment at 180 °C for 4 h and a second treatment at 300 °C for 4 h. This heat-treatment is to avoid clogging of the fuel feeding system of the experiment pilot while keeping the ash-rich property. After pretreatment, the proximate and ultimate analyses of the fuel were made and are shown in Table 2. Obviously, the pretreated microalgae have a lower volatiles which may shift the CLG performance as compared to the untreated microalgae. But the pretreatment retains the high-ash property of the microalgae, and this is a main concern of the current study, among others including the comparatively high nitrogen levels relative to lignocellulose biomasses. On the other hand, the low volatile content can lessen the effect of volatiles on the reactions, and highlights the gasification reaction itself, thus offering a better basis for comparison of different oxygen carriers. To analyze the ash composition, the ash was produced by air oxidation at 550 °C according to the ISO 18122:2022 standard [35], and subject to analyses with Inductively Coupled Plasma Optical Emission Spectroscopy (ICP-OES). The microalgae contain high levels of potassium, phosphorus and sodium, which, while catalyzing the gasification reaction, could also lead to slagging and agglomeration in the reactor [18].

2.2. 1.5 kW_{th} CLG unit at ICB-CSIC

The experimental campaign was carried out with the 1.5 kW_{th} chemical looping unit at ICB-CSIC research center in Zaragoza, Spain. A schematic overview of the system is shown in Fig. 2. The facility is

Table 2
Properties of the pretreated microalgae used in this work and of the original microalgae.

Analysis		Original microalgae	Pretreated microalgae (used in this work)
Proximate analysis/ wt% (as received basis)	Moisture	10.1	5.4
	Ash	5.9	12.5
	Volatile matter	71.8	37.0
	Fixed carbon (By difference)	12.2	45.2
Ultimate analysis/wt % (as received basis)	Carbon	45.2	54.7
	Hydrogen	7.1	3.2
	Nitrogen	10.2	12.9
	Sulfur	0.8	0.9
	Oxygen (By difference)	30.8	10.5
Ash composition (mg/(kg biomass), as received basis)	Ca	1221	1044
	P	8425	7611
	Fe	643	861
	Mg	2649	2442
	K	13,275	14,278
	Na	3858	4189
Properties	LHV (MJ/kg microalgae, as received basis)	20.2	20.5
	Ω_b (mol O/kg microalgae, as received basis)	97.9	108.8

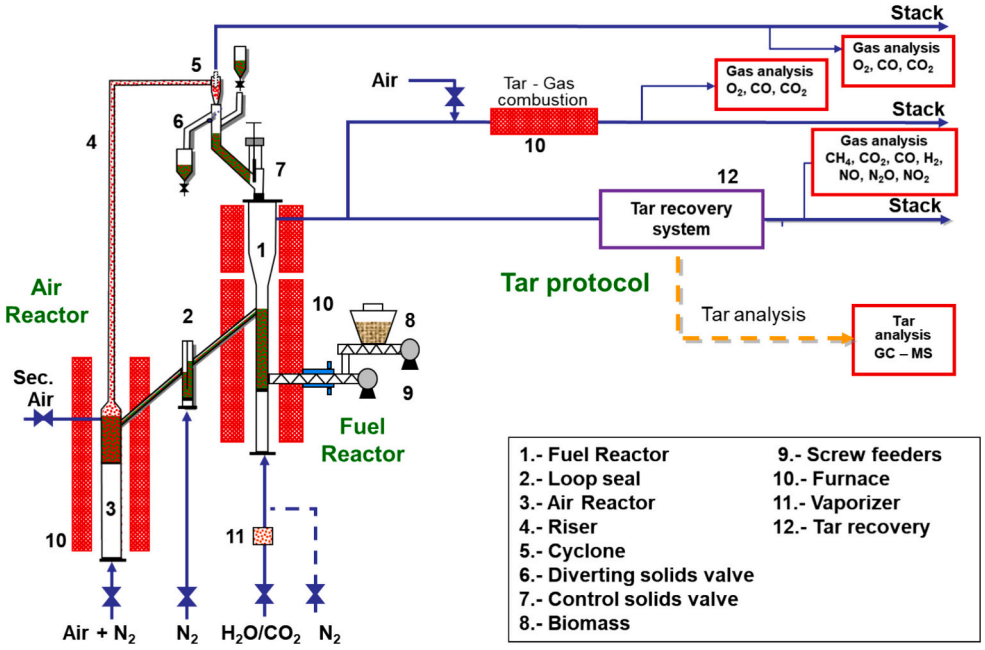


Fig. 2. Scheme of the 1.5 kW_{th} unit at ICB-CSIC.

composed by two fluidized beds acting as the FR and AR, whose bottoms are connected through a loop-seal and tops are connected through a solid value which acts as an upper loop-seal and a controller of solids circulation rate. These devices enable a continuous solids transfer, a regulated solids circulation, while preventing the gas mixing. The FR and AR reactors are electrically heated with electric ovens, and the temperature in each reactor can be separately controlled and adjusted. The total OC inventory introduced for each set of experiments was 2.5 kg. Prior to the gasification tests, the materials were circulated in air at 850 °C for several hours to reach stable fluidization and circulation states.

The unit is equipped with a two-stage fuel feeding system that was designed to avoid premature decomposition of fuel before entering the reactor. The microalgae are stored in a stainless-steel chamber and the feeding rate is regulated by a primary screw feeder. The secondary screw feeder is equipped with a water-cooling jacket and operated at high-speed to convey fuel rapidly into the FR. In this way, fuel pyrolysis in the feeding system is hugely minimized. The FR was fluidized with steam, CO_2 or mixtures of steam and CO_2, depending on the operation condition. The steam was generated by feeding a certain flow of water through a heated vaporizer at 150 °C. The AR was fluidized with a mixture of air and N_2, where the flows of air and N_2 were carefully selected according to the desired oxygen to fuel ratios. In this way, the oxygen supplied is well controlled by the oxygen flow, instead of the total gas flow, entering the AR, and the oxygen can be fully consumed by the oxygen carrier. This method allows an accurate control of the oxygen amount transferred to the FR [36]. The loop seal (LS) received an independent supply of N_2 (90 NL/h) to maintain a stable solids flow and to avoid back-mixing. The total gas flow to the FR was set to 130 NL/h for all tests, and the typical gas flow to AR is 2100 NL/h except when using iron sand which has a lower density and thus a lower AR gas flow.

The concentration of outlet gases from both AR and FR were monitored continuously with gas analyzers. The FR stream was divided into two branches. One branch was directed to a high-temperature post-combustor, where the gas was oxidized with high purity O_2. The second branch was first sent to a tar-collection train where the tar was sampled according to a European protocol [37] and analyzed with GC–MS combination technique [38]. The tar-collection train consisted of eight bottles connected in series. The first two bottles were maintained at approximately 0 °C to condense and remove water, avoiding blockage caused by ice formation, and the subsequent six bottles were filled with isopropanol and kept at around −20 °C for efficient tar condensation and collection. The tar collection was conducted under steady-state operation for 1 h in selected tests. After collection, the condensates and solutions from the eight bottles were combined, diluted and subject to Gas Chromatography–Mass Spectrometry (GC–MS) analysis for speciation and quantification of individual tar compounds. The total tar yield was calculated by dividing the sum of all quantified species with the feeding rate of the pretreated microalgae. After the tar sampling train, the dry gas from the FR was passed through on-line analyzers for measuring the CO_2, CO, CH_4 and H_2 concentrations. In addition, the FR gas were periodically sampled and analyzed with a PerkinElmer GC analyzer to analyze the concentration of light hydrocarbons. In the case of the ilmenite campaign, NOx gas composition (NO, N_2O and NO_2) was also analyzed with a Pfeiffer quadrupole mass spectrometer [39]. Gas leaving the AR was sent to an online analyzer to measure the O_2, CO and CO_2 concentrations.

The test sequence for each OC followed a consistent procedure. After the stabilization phase in air flow, the FR fluidization stream was switched to steam-based gasification medium while the feeding of microalgae commenced. The gas flow, gasifying agent (H_2O or CO_2) and other reacting conditions were changed when needed. Data acquisition was conducted throughout the entire experimental process. For each oxygen carrier, a campaign of 4–5 days was managed. At the end of each day, the reactor vessels were cooled down with a flow of air. Solid samples were collected intermittently from both reactors and the cyclones, and subject to several characterizations including physico-chemical properties through X-ray diffraction (XRD), Inductively Coupled Plasma Optical Emission Spectroscopy (ICP-OES) and Scanning Electron Microscopy coupled with Energy Dispersive X-ray Spectroscopy (SEM-EDX) as well as reactivity with 15%H_2 at 950 °C in a Thermogravimetric Analyzer (TGA).

2.3. Experimental conditions

The experimental campaign was structured to evaluate the gasification performance of microalgae under a wide range of reacting conditions. For each OC, 50–70 h of hot operation were conducted and the

operation with microalgae lasted 20–25 h. The experiments were divided into three main groups: (i) assessment of the influence of the oxygen-to-fuel ratio (λ) under steam gasification, (ii) test of different FR temperatures at a fixed λ, and (iii) evaluation of different gasification atmospheres at a fixed operating temperature. A summary of all operating conditions is provided in Table 3.

In the groups of Test 1–5, Test 8–13 and Test 16–18, the FR was fluidized solely with steam, while the oxygen-to-fuel ratio was controlled by adjusting the flow of air fed to the AR, as detailed above. For ilmenite and LD slag, the total AR flow (air + N_2) was kept at 2100 NL/h. For iron sand, there were some adjustments in the N_2 flow to maintain a lower total flow to facilitate the particles fluidization and circulation. This is because the iron sand has a lower bulk density as compared to ilmenite and LD slag. Despite the different total gas flow with iron sand, the oxygen flow entering with air was kept identical to those used for ilmenite and LD slag, and this ensures a same oxygen transfer rate and thus the effective oxygen-to-fuel ratio remained consistent with the campaigns with LD slag and iron sand. For each OC, three oxygen-to-fuel ratios were tested at different FR temperatures. It should be noted that some of the microalgae feeding rates were slightly different from another (e.g., 61.3 vs 59.3 and 59.2 vs 56.5), because the experiments were done in different days and the fuel feeding condition was changed slightly. But, in our opinion, this slight change would not cause big influence to the results. In the group of Tests 5–7, 9, 14, 15, 19 and 20, influence of the gasification agent composition was studied at a fixed temperature. Three compositions were evaluated while we maintained a constant flow rate to the FR with the H_2O:CO_2 ratios of 100:0, 50:50, and 0:100. Despite the different composition, the overall gasification agent to fuel ratio was kept roughly at a (H_2O + CO_2)/C molar ratio of 2.1 and in the case of only steam this ratio is translated to a steam to biomass mass ratio (which is usually expressed as S/B) of 1.5. This experimental setting enables us to study the effect to the CLG performance when changing gasification agents from steam to carbon dioxide.

2.4. Reactions in the BCLG system

Table 4 lists the principal reactions considered in the reacting system using Me_xO_y as a substitution of the OCs. The microalgae conversion begins with devolatilization in FR, producing volatiles, tar vapors, water vapor and char (R1). The char subsequently reacts with steam and CO_2 through normal gasification routes, generating CO and H_2 (R2 and R3). Gases from microalgae decomposition and char gasification mainly include CO, H_2 and CH_4, and they subsequently are oxidized partly or fully by Me_xO_y while the OC is reduced to Me_xO_{y-1} (R4-R7). Extent of these reactions determines the gasification product composition and the rate of oxygen transfer. In addition, methane reforming can proceed through steam (R8) and dry reforming (R9) reactions. Also, the CO may further be converted through water-gas shift reaction (R10). Tar compounds can be decomposed thermally and oxidized by the Me_xO_y, and this further contributes to syngas production (R11-R14). In AR, the reduced OC (Me_xO_{y-1}) is oxidized back to Me_xO_y by the gaseous O_2 in air (R15). In some cases, unconverted char may enter AR through the loop seal, and be oxidized to CO_2 in the AR through reaction (R16).

Table 4
Principal reactions in the BCLG system using Me_xO_y and Me_xO_{y-1} as substitutions (see Table 1 for phases of the oxygen carriers).

Type	Reactions
Microalgae decomposition	Microalgae → volatiles + tar + char + vapor (R1)
Char gasification with H_2O	$C + H_2O \rightarrow CO + H_2$ (R2)
Char gasification with CO_2	$C + CO_2 \rightarrow 2CO$ (R3)
Reduction of OC by the gases	$Me_xO_y + H_2 \rightarrow Me_xO_{y-1} + H_2O$ (R4)
	$Me_xO_y + CO \rightarrow Me_xO_{y-1} + CO_2$ (R5)
	$4Me_xO_y + CH_4 \rightarrow 4Me_xO_{y-1} + CO_2 + 2H_2O$ (R6)
	$Me_xO_y + CH_4 \rightarrow Me_xO_{y-1} + CO + 2H_2$ (R7)
CH_4 reforming reactions	$CH_4 + H_2O \rightarrow 3H_2 + CO$ (R8)
	$CH_4 + CO_2 \rightarrow 2H_2 + 2CO$ (R9)
Water-gas shift reaction	$CO + H_2O \leftrightarrow CO_2 + H_2$ (R10)
Tar reactions	Tar → $CO + H_2 + C_xH_y$ (R11)
	Tar + $H_2 \rightarrow CH_4/C_xH_y$ (R12)
	Tar + $H_2O/CO_2 \rightarrow CO + H_2$ (R13)
	Tar + $Me_xO_y \rightarrow Me_xO_{y-1} + CO_2 + H_2O$ (R14)
Oxidation (regeneration) of OC in AR	$2Me_xO_{y-1} + O_2 \rightarrow 2Me_xO_y$ (R15)
Oxidation of char in AR	$C + O_2 \rightarrow CO_2$ (R16)

3. Data processing

The oxygen to biomass ratio (λ) is the ratio between the amount of oxygen transferred by the OC and the stoichiometric oxygen for complete combustion of the microalgae. In the experiments, the oxygen fed into the AR is all taken to the FR and transferred by the OC, and no or little carbonaceous gases were seen at the AR exit, so the oxygen-to-fuel ratio can be calculated through the equation below.

Table 3
Experimental conditions of continuous operations of the 1.5 kW_{th} unit with microalgae.

OC	Test	T_{FR} (°C)	$(Air/N_2)_{AR}$ (NLh^{-1}/ NLh^{-1})	Microalgae feeding, F_b(g/h)	λ	$(Steam/CO_2)_{FR}$ (NLh^{-1}/ NLh^{-1})	H_2O:CO_2 ratio in FR
Ilmenite	1	920	50/2050	71.8	0.13	130/0	100:0
Ilmenite	2	920	100/2000	71.8	0.26	130/0	100:0
Ilmenite	3	920	150/1950	71.8	0.39	130/0	100:0
Ilmenite	4	860	100/2000	61.3	0.30	130/0	100:0
Ilmenite	5	920	100/2000	59.3	0.31	130/0	100:0
Ilmenite	6	920	100/2000	59.3	0.31	65/65	50:50
Ilmenite	7	920	100/2000	59.3	0.31	0/130	0:100
LD slag	8	920	50/2050	54.2	0.18	130/0	100:0
LD slag	9	920	100/2000	54.2	0.29	130/0	100:0
LD slag	10	920	150/1950	54.6	0.51	130/0	100:0
LD slag	11	860	100/2000	62.1	0.30	130/0	100:0
LD slag	12	860	100/2000	62.1	0.30	130/0	100:0
LD slag	13	890	50/2050	62.1	0.15	130/0	100:0
LD slag	14	920	100/2000	54.6	0.34	65/65	50:50
LD slag	15	920	100/2000	54.6	0.34	0/130	0:100
Iron sand	16	920	100/900	56.5	0.33	130/0	100:0
Iron sand	17	880	150/700	56.5	0.49	130/0	100:0
Iron sand	18	860	100/1450	59.2	0.31	130/0	100:0
Iron sand	19	890	100/800	56.5	0.33	65/65	50:50
Iron sand	20	890	100/1800	56.5	0.33	0/130	0:100

$$\lambda = \frac{2F_{O_2,AR,in}}{F_b \Omega_b} \quad (1)$$

The Ω_b is the stoichiometric oxygen for full combustion of the microalgae (mol O/kg microalgae), and it was calculated based on the microalgae's ultimate analysis, through Eq. (2) below. Values of the original and pretreated microalgae are displayed in Table 2.

$$\Omega_b = \left(\frac{8}{3}x_C + 8x_H + x_S - x_O\right)\frac{1000}{16} \quad (2)$$

where x_i values are based on the ultimate analysis of the pretreated microalgae, as seen in Table 2.

The BCLG performance with microalgae was analyzed with several indicators such as biomass conversion, syngas yield, and cold gas efficiency (CGE, η_g). The biomass conversion (X_b) reflects the mass fraction of microalgae converted in the AR and FR vessels, and is calculated by considering the flows of carbon-containing gases leaving the two reactors and the microalgae feeding rate.

$$X_b = \frac{F_{C,FR,out} + F_{C,AR,out}}{F_{C,b}} \quad (3)$$

$$F_{C,b} = \frac{1}{12}F_b x_C \quad (4)$$

$$F_{C,FR,out} = \left[F_{CO_2} + F_{CO} + F_{CH_4}\right]_{FR,out} \quad (5)$$

$$F_{C,AR,out} = F_{CO_2,AR,out} \quad (6)$$

Carbon emitted from AR ($C_{AR,emit}$) is defined as the proportion of carbon (mainly in the form of CO_2) leaving the AR over the total carbonaceous gases from the AR and FR.

$$C_{AR,emit} = \frac{F_{C,AR,out}}{F_{C,FR,out} + F_{C,AR,out}} \quad (7)$$

Syngas yield (Y, Nm^3/kg of dry microalgae) is defined as the sum of the standard volume flows of H_2 and CO generated from per kilogram dry biomass fed into the system.

$$Y = Y_{H_2} + Y_{CO} = \frac{G_{H_2}}{F_{b,dry}} + \frac{G_{CO}}{F_{b,dry}} \quad (8)$$

The H_2/CO molar (or volumetric) ratio is used to show the relative selectivity of H_2 and CO in the syngas, and this is useful when evaluating the applicability of the syngas in intended industry processes.

$$\frac{H_2}{CO} = \frac{Y_{H_2}}{Y_{CO}} \quad (9)$$

The CGE (η_g) is defined as the ratio of the chemical energy in the FR product gas over the total energy content of the microalgae.

$$\eta_g = \frac{F_{CO}\Delta H_{comb,CO} + F_{H_2}\Delta H_{comb,H_2} + F_{CH_4}\Delta H_{comb,CH_4}}{F_b LHV_b} \quad (10)$$

The gas concentrations are normalized by removing the dilution by steam and background nitrogen gas through the equation below to get the dry-and-nitrogen free gas concentrations (x_{dnf}). This parameter facilitates comparing among the oxygen carriers.

$$\chi_{dnf} = \frac{\chi_i}{\sum \chi_i} \quad (11)$$

Fuel nitrogen conversion (X_{fn}) is defined to reflect how the microalgae nitrogen is converted and distributed relatively in the nitrous gas products.

$$X_{fn} = \frac{F_{NO_x}}{F_{Nfuel,in}} \quad (12)$$

The data from TGA characterization is processed to calculate the OC conversion in the reduction (X_r), and oxidation (X_o) through Eqs. (13) and (14), and these were further used to get the (*rate index*)$_{TGA}$ index [34,40] (see Eq. 15) to quantify the material reactivity in reduction with H_2.

$$X_{r,OC} = \frac{m_o - m}{R_{OC} m_0} \quad (13)$$

$$X_{o,OC} = \frac{m - m_r}{R_{OC} m_0} \quad (14)$$

$$(\text{Rate index})_{TGA} = 100 \times 60 \times R_{OC} \times \left(\frac{dX_{r,OC}}{dt}\right)_{norm} \quad (15)$$

where the constants 100 and 60 are used to unify the unit of the final results to %/min, $(dX_{r,OC}/dt)_{norm}$ was calculated through eq. (16) with the assumption of a first-order reaction between the OCs and H_2 [40]. And thus, the $(dX_{r,OC}/dt)_{exp}$ was derived from the liner part of the $X_{r,oc}$-t curves at the beginning of reactions.

$$\left(\frac{dX_{r,OC}}{dt}\right)_{norm} = \frac{p_{ref}}{p_{TGA}} \times \left(\frac{dX_{r,OC}}{dt}\right)_{exp} \quad (16)$$

where p_{ref} is fixed to 0.15 atm and p_{TGA} is 0.15 in current work.

4. Results

4.1. Overall reaction progress

Fig. 3 presents the temporal evolution of the major gas species from the FR—CO_2, H_2, CO, and CH_4—during representative operation days with the three OCs. The concentrations were recorded continuously from the moment when the fuel feeding was started until the end of the day. Take Fig. 3(a) as an example (using fully oxidized ilmenite as the start material), before the fuel was started, the temperature, AR fluidization gases, FR fluidized gases and other parameters were all well-tuned to desired conditions, thus building a period/start point where the gas concentrations are zero. At the onset of fuel start, a sharp peak of CO_2 concentration is observed, while the formation of syngas species (H_2, CO) is negligible. This behavior shows that the lattice oxygen retained in the ilmenite at the beginning is abundant, and the oxygen oxidizes immediately the fuel, so there is a nearly complete combustion (only CO_2 is seen) in the early stage. This initial period therefore corresponds to the CLC (chemical looping combustion) regime. After around 10 min of combustion, the CO_2 concentration decreases gradually while a rise in the H_2 and CO concentrations is seen. This transition marks the reaction was shifted from CLC to CLG, when the OC was progressively reduced to a stable state where the rate of oxygen transfer was limited by the oxygen supply. After this transition period the system reached a steady stage where the CLG process with relatively stable CO and H_2 dominates. Throughout the progress, the CH_4 remained low and nearly constant, with a concentration of around 1%. The CH_4 is from the microalgae volatiles which have insufficient contact time to react with the OC, and thus part of it bypassed the bed. In the case of LD slag and iron sand, there are several periods where all the concentration is near zero. This is because we stopped the gas analyses to clean the gas sampling channels or were switching the condenser to/from the tar collection train.

Fluctuation is normal in fluidized-bed systems, and a clear difference of the fluctuation degree is seen among the OCs. LD slag exhibits the least fluctuation and has smooth and steady gas-composition profiles throughout the experiments. Ilmenite also shows a low fluctuation. Iron sand, however, has a high fluctuating gas profile, especially in the fully developed CLG stage. The large fluctuation is attributed to the relatively lower bulk density of iron sand, which could be quite sensitive to the fluidization in the FR. Quasi-steady time-averaged was applied to the concentration to minimize the effect of fluctuation. The larger fluctuation observed with iron sand is interesting and requires more detailed

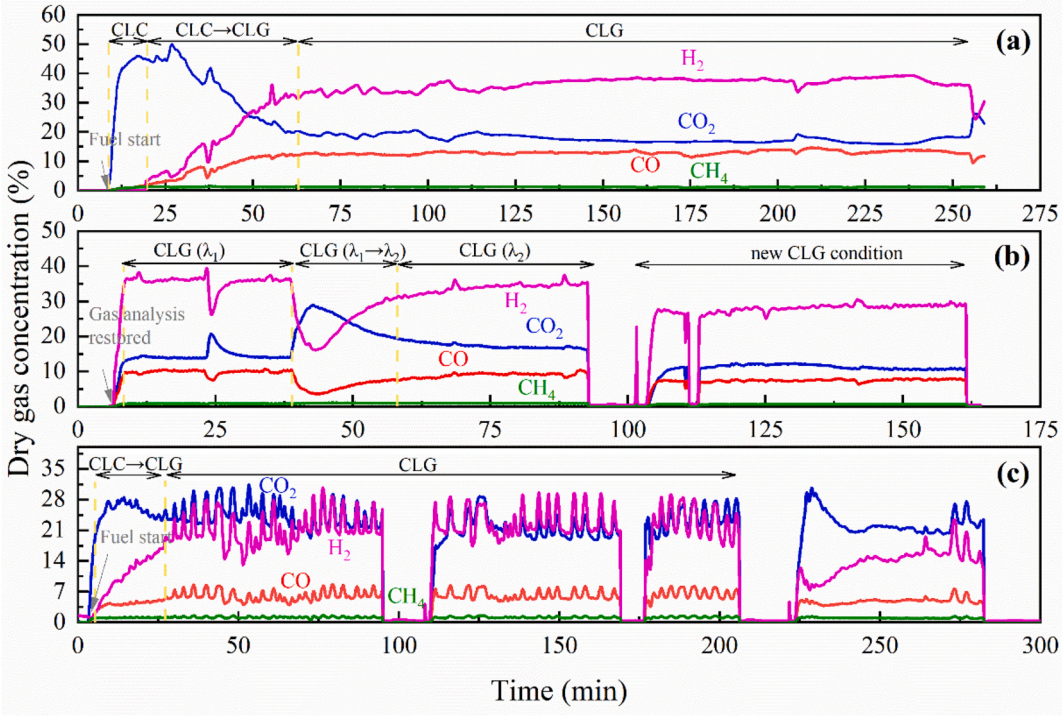


Fig. 3. Concentration profile of main gases from the FR during typical operations (a) using ilmenite, (b) using LD slag, and (c) using iron sand at T_{FR} = 890–920 °C. The "fuel start" means when we saw gases through the gas analyzers after we started the microalgae feeding, and the "gas analysis restored" means the analyzers are connected to the data log after an interruption.

studies. This property may influence negatively the operational robustness and thus the syngas quality during prolonged campaigns in larger scale systems. Optimization of the iron sand particle properties, fluidization conditions, and solids circulation may therefore be necessary for future large-scale applications.

4.2. Effect of operating conditions

In this section, the influence of three key operating parameters—oxygen-to-fuel ratio (λ), FR temperature, and gasifying agent—on the BCLG performance with the three OCs is evaluated. The analysis provides a comprehensive assessment of how the operating conditions affect microalgae conversion, syngas composition, gas selectivity and overall process efficiency.

4.2.1. Effect of oxygen-to-biomass ratio (λ)

Table 5 summarizes the effect of oxygen-to-fuel ratio on the microalgae conversion (X_b) and carbon emitted from AR ($C_{AR,emit}$). It should be noted that although Test 17 has a lower temperature (880 °C) than other comparing cases (920 °C), the effect of temperature on iron sand is proved not relevant and the performance is rarely affected by temperature, see Figs. 6 and 7. In most cases, the microalgae conversion is close to 100%, which indicates that almost all the fuel was converted in the system (either in FR or AR) and little left the system in the form of residual char. The carbon emitted from AR is near 0%, and this means the microalgae had little or no leak from FR to AR. It is also notable that slightly low conversions (X_b is around 82%) are seen with ilmenite, so some unconverted char was found in the FR cyclone when we made post-run inspections and system clean-up. In few isolated cases, the carbon emitted from AR went up to 3.5%, so some CO_2 was detected at the AR outlet. This minor breakthrough likely because some unreacted microalgae particles were carried to the AR, and there they were oxidized to CO_2 (R16).

Table 5
Effect of oxygen-to-fuel ratio on the microalgae conversion (X_b) and carbon emitted from AR ($C_{AR,emit}$), and the condition is T_{FR} = 920 °C (except Test 17 whose temperature is 880 °C) and 100% steam.

	Ilmenite		LD slag			Iron sand	
	Test 1	Test 2	Test 8	Test 9	Test 10	Test 16	Test 17
λ	0.13	0.26	0.18	0.29	0.51	0.33	0.49
X_b (%)	82.0	92.2	100.0	100.0	100.0	98.2	100
$C_{AR,emit}$ (%)	0	3.5	0	0	0	2.1	0

Fig. 4 illustrates the influence of oxygen-to-fuel ratio on the major gas species from the FR. As λ increases, the CO_2 concentration rises greatly, whereas the H_2 and CO concentrations decline and CH_4 remains nearly unchanged, and these trends agree well with results in the previous works [36,41]. This behavior is attributed to the shift of dominant reaction pathways. At a higher λ, a larger amount of lattice oxygen is transferred into the FR through the circulating OC, which promotes the full oxidation of the devolatilization products, gasification products and reforming intermediates. Consequently, the combustion reactions (R4-R6) become dominant. The depletion of H_2 and CO with increasing λ therefore is a result of the enhanced contribution of oxidation routes, which convert these species into CO_2 and H_2O. Meanwhile, we compared with literature data from pine wood BCLG with ilmenite in the same unit [41], see dashed lines in Fig. 4(a). The current work used heat-treated microalgae that have little volatile (thus little CH_4), so the H_2 concentration is much higher than in the previous work where a high volatile pine wood was used [41]. Overall, these results confirm that increasing λ shifts the FR atmosphere toward more oxidative conditions, resulting in lower syngas quality and higher CO_2 formation, whereas a low λ is favorable for syngas enrichment.

Fig. 5 illustrates the influence of the oxygen-to-fuel ratio on key indicators of the syngas production performance. For all the three OCs, both the CGE and syngas yield exhibit a consistent decreasing trend with the increase of λ. This decline results in the compositional shifts as

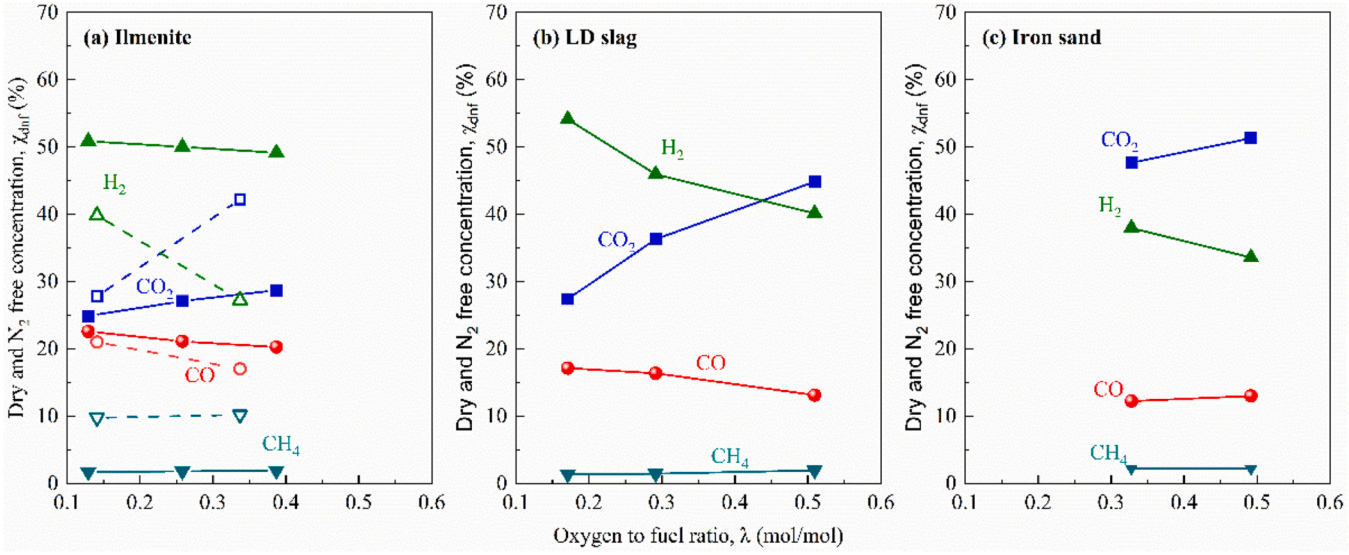


Fig. 4. Effect of the oxygen-to-biomass ratio (λ) on gas composition (dry and N_2 free concentrations) in gasification with 100% steam. Data with filled dots are from Test 1, 2, 3 for ilmenite, Test 8, 9, 10 for LD slag and Test 16, 17 for iron sand at T_{FR} = 920 °C (except Test 17 whose temperature is 880 °C, and the effect of temperature is small, see Figs. 6 and 7 below) and data with void dots are from previous work [41] with ilmenite and pine wood pellets at T_{FR} = 940 °C and steam-to-biomass ratio of 0.6.

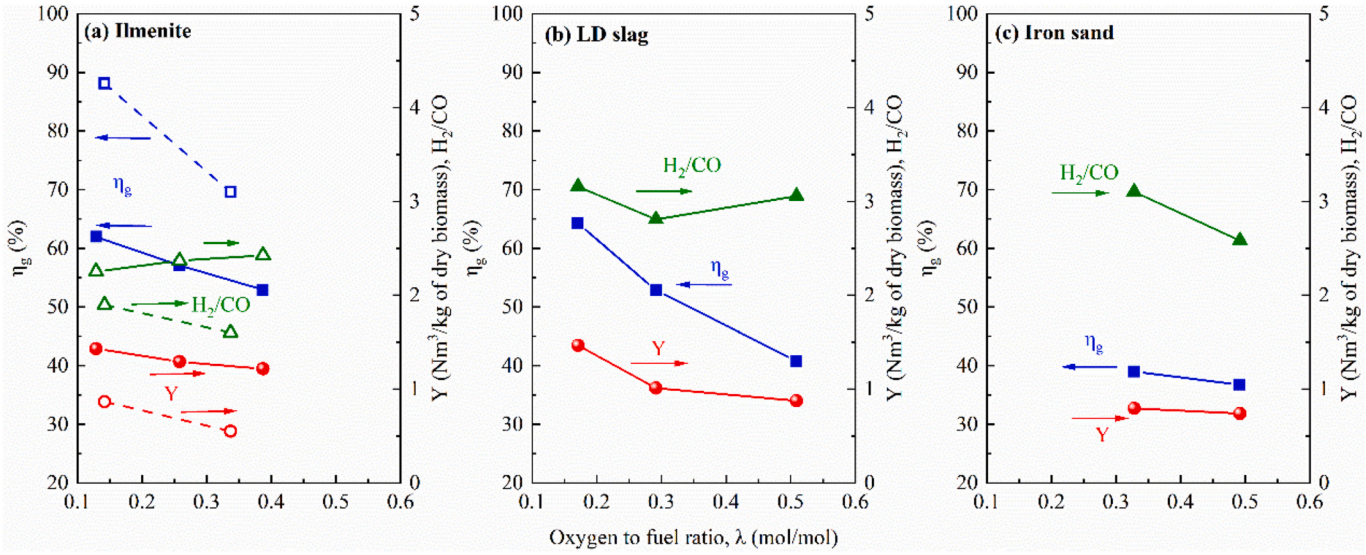


Fig. 5. Effect of oxygen-to-biomass ratio (λ) on η_g, Y and H_2/CO ratio during the gasification with 100% steam. Data in filled dots are from Test 1, 2, 3 for ilmenite, Test 8, 9, 10 for LD slag and Test 16, 17 for iron sand at T_{FR} = 920 °C (except Test 17 whose temperature is 880 °C, and effect of temperature is negligible see Figs. 6 and 7 below) and the data with void dots are from previous work with ilmenite and pine wood pellets at T_{FR} = 940 °C and steam-to-biomass ratio of 0.6 [41].

discussed earlier. As more oxygen is carried to the fuel reactor, a larger fraction of the fuel undergoes oxidation rather than gasification. This lowers the syngas production and CGE, thus reducing the chemical energy extracted from the microalgae. Again, the syngas yield with the heat-treated microalgae is much higher than that with pine wood pellets [41], as a result of the different volatiles content. Regarding the H_2/CO ratio, the values observed across all OCs remain within the range of 2.3–3.2. Notably, this ratio does not show clear dependence on λ, especially for LD slag. Although syngas with elevated H_2/CO ratios can still be utilized for FT synthesis, excessive hydrogen may suppress the hydrocarbon chain growth and reduce selectivity toward long-chain hydrocarbons [42]. This highlights the importance of controlling downstream conditioning processes (e.g., CO_2 removal, WGS adjustment) to tailor the syngas composition for an optimal FT performance.

4.2.2. *Effect of FR temperature*

The effect of FR temperature was investigated at 860 °C and 920 °C which covers the common range for CLG process, and the effect on the microalgae conversion and carbon emitted from AR is summarized in Table 6. Consistent with the analysis in the previous section, the ilmenite

Table 6
Effect of FR temperature (T_{FR}) on biomass conversion (X_b) and carbon emitted from AR ($C_{AR,emit}$), gasification with steam at $\lambda \approx 0.3$.

	Ilmenite		LD slag		Iron sand	
	Test 4	Test 5	Test 11	Test 9	Test 18	Test 16
	860 °C	920 °C	860 °C	920 °C	860 °C	920 °C
X_b (%)	82.7	83.7	99.2	100	100	100
$C_{AR,emit}$ (%)	2.9	0	0	0	0	0

has microalgae conversions below 100%. As the FR temperature increases, the microalgae conversion is improved, reaching 83.7% in the case with ilmenite. This is attributed to faster reaction kinetics at elevated temperatures [43]. In contrast, the microalgae are all converted in the FR side; thus 0% carbon were emitted from the AR, indicating that the LS worked well in these conditions.

Fig. 6 presents the influence of FR temperature on the main gas species from the FR. For ilmenite, an increase in both CO and CO_2 concentrations is observed with the increase of temperature. This behavior may be attributed to simultaneous enhancement in char gasification and oxygen transfer reactions at elevated temperatures. While higher temperatures promote CO and H_2 formation through gasification, they may also facilitate the oxidation of H_2 and CO by the OC. In the case of LD slag, the temperature increase promotes more the gasification than oxidation, thus there is more H_2 and CO and less CO_2 at 920 °C as compared to 860 °C. This behavior may be a result of the high calcium content (in form of CaO) in LD slag, which is a catalyst and promotes more significantly the gasification at a higher temperature [44–46]. The catalytic effect of CaO becomes more pronounced at elevated temperatures, leading to enhanced char gasification and consequently higher syngas production. Therefore, both CO and H_2 concentrations increase simultaneously when using LD slag as oxygen carrier. The CaO is also a catalyst on the WGS reaction, and it can catalyze the reaction toward the direction favoring more H_2 production [46,47], but may be not very effective at such high temperatures in CLG process. Moreover, the reversible carbonation/decarbonation behavior of Ca-containing phases may contribute to further lowering the CO_2 concentration through carbonation in lower-temperature zones (e.g., FR cyclone) of the system, and this could further benefit H_2 formation. Different to LD slag and ilmenite, the iron sand was almost not affected by the temperature increase, and this might be a result of similar promotion of temperature on the gasification and oxidation by the OC. The ilmenite and LD slag have H_2 and CO_2 concentrations in a similar interval, whereas the iron sand's H_2 concentration is lower and CO_2 concentration is higher as compared to the other two OCs. The special H_2 and CO_2 concentrations with iron sand might be because of the iron sand's relatively higher reactivity with H_2 and CO as compared to LD slag and ilmenite [48]. Therefore, much of the H_2 and CO generated from gasification may be oxidized to water vapor and CO_2 by the OC, and after the vapor condensation and gas concentration normalization, CO_2 showed a higher dry-and-N_2 free concentration than H_2.

Fig. 7 shows the effect of FR temperature on CGE, syngas yield, and the H_2/CO ratio. For all the three OCs, both the CGE (η_g) and H_2/CO ratio decrease with the increase of FR temperature (and slight increase in η_g is seen with LD slag may be due to experiment uncertainties). Iron sand has the lowest CGE, and it drops from 42.3% to 39.0% with the temperature increase from 860 to 920 °C, whereas the ilmenite and LD slag maintain a higher efficiency in the range of 52.2% to 47.0% and 52.8% to 52.9%, respectively. The H_2/CO ratio of all the OCs is in the range between 2.5 and 3.3, with significant decrease for ilmenite and LD slag, and almost not changes for iron sand. The decrease of H_2/CO ratio shows clearly that the increase of temperature is not favorable for the H_2 generation, which maybe a result of a higher reactivity of H_2 as compared to CO with the OCs (ilmenite and LD slag). Syngas yield is relatively constant with increasing FR temperature for the three OCs.

4.2.3. *Effect of gasification agent*

Fig. 8 illustrates the effect of the type of gasification agent on the microalgae conversion and carbon emitted from AR. When 100% steam was used as the gasification agent, the microalgae conversion is at consistently high levels for all the OCs and no carbon emission from the AR, indicating that steam promotes effectively the char gasification. In contrast, when adding 50% CO_2 to the gasification agent and using 100% CO_2, the microalgae conversion goes down and the carbon emitted from AR increases. This can be attributed to the slower kinetics of the CO_2 gasification as compared to the steam gasification. Also, the catalytic activity of alkali metals over the char gasification is usually lower in CO_2-rich atmospheres, as compared to the gasification with steam, and this was seen in our recent kinetics studies for microalgae char gasification [43]. The effect of gasification agent is particularly clear for iron sand, where the biomass conversion dropped close to 50% and carbon emitted went to 17% when gasifying with 100% CO_2. We also confirmed the insufficient gasification with iron sand and 100% CO_2 when cleaning the unit, and found accumulations of unconverted char in the FR cyclone. For this reason, we don't suggest to use pure CO_2 as gasification agent for large scale CLG process with microalgae and these oxygen carriers. It should be noted that the suitability/unsuitability of pure CO_2 as gasifying agent depends on both biomass properties and OC characteristics, and therefore the present conclusion should not be generalized to all CLG systems.

The effect of gasification medium on the main gas species in the FR is shown in Fig. 9. For all three OCs, a consistent evolution of gas composition is observed as steam is replaced by CO_2. In steam conditions, high concentration of H_2 is usually attained and this is promoted

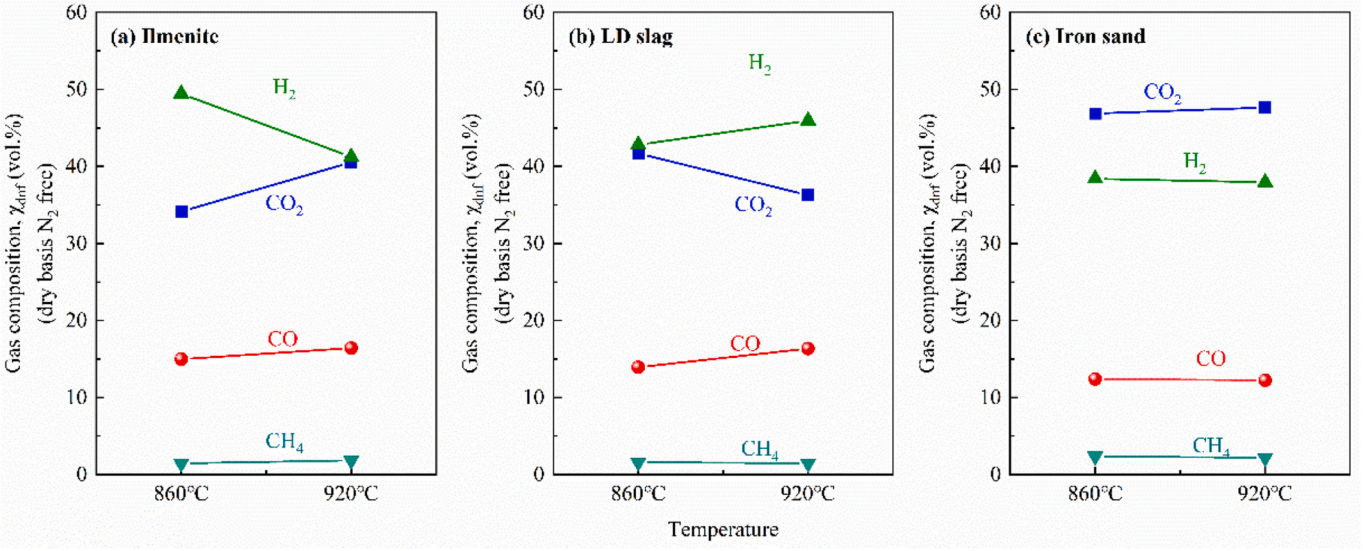


Fig. 6. Effect of FR temperature (T_{FR}) on the dry and N_2 free gas concentrations with the three OCs in 100% steam gasification and oxygen-to-biomass ratio of $\lambda \approx 0.3$. Data of ilmenite are from Test 4 and 5. LD slag from Test 9 and 11, and Iron sand from Test 16 and 18.

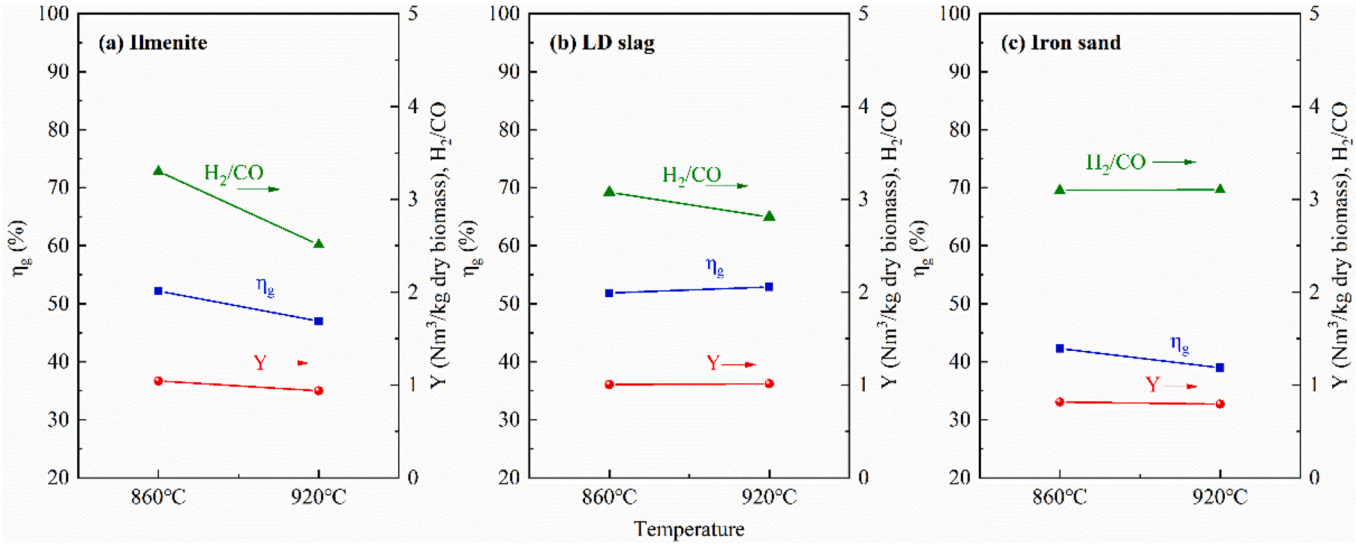


Fig. 7. Effect of FR temperature (T_{FR}) on η_g, Y and H_2/CO when λ is around 0.3 and the gasification was with 100% steam. Data of ilmenite are from Test 4 and 5, LD slag from Test 9 and 11, and Iron sand from Test 16 and 18.

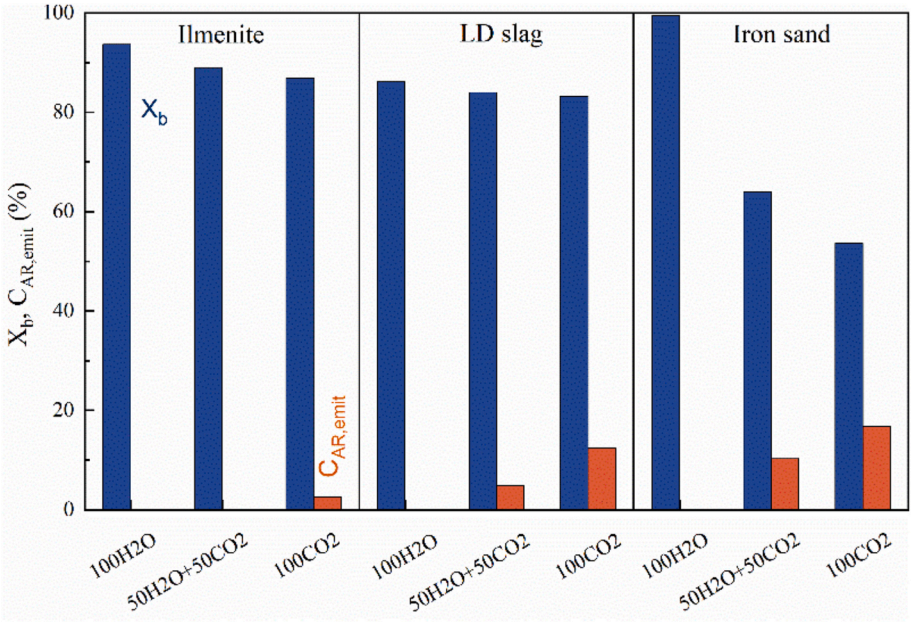


Fig. 8. Effect of gasification agent on the microalgae conversion (X_b) and carbon emitted from AR ($C_{AR,emit}$), λ ≈ 0.3, T_{FR} = 920 °C (except Test 19 and 20 which have a temperature of 890 °C). Results are from Test 5, 6 and 7 for ilmenite, Test 9, 14 and 15 for LD slag and Test 16, 19 and 20 for iron sand.

primarily by the char gasification with steam (R2) and the water gas shift reaction (R10). As the availability of steam decreases as a result of replacement with CO_2, both the steam gasification and WGS reactions are suppressed, resulting in a huge reduction in H_2 production. Simultaneously, the dry gasification (R3) becomes more favored under CO_2-rich conditions, explaining the increase of CO concentration.

The influence of the gasification agent on the syngas yield, cold gas efficiency and H_2/CO ratio is shown in Fig. 10. Obviously, when CO_2 is added to the gasifying atmosphere, the CO increases and H_2 decreases, thus the H_2/CO ratio goes down quickly and approaches near zero when the CO_2 concentration is 100%. The total syngas yield with ilmenite and iron sand went down gradually when switching the gasifying gas from 100% steam to 100% CO_2, while the gas yield with LD slag is not so sensitive to the composition of gasification agent. Similar to the trend of gas yield, the cold gas efficiency also goes down with ilmenite and iron sand, and the trend with LD slag seems not only going down.

4.2.4. *Tar and NO_x analysis*

As shown in Fig. 11, the total tar yield ranges from 0.5 to 1.2 g/kg dry biomass, while in the same pilot the tar yield is 3.5–4.5 g/kg with LD slag and several biomasses [28] and 1.3–2.8 g/kg with ilmenite and pine wood pellets [41]. But it is hard to compare between the microalgae and these biomasses, because during the pretreatment the microalgae lost most of volatiles which could have a significant contribution to tar yield and the total tar yield could be higher if the raw microalgae were used. When gasifying with a similar oxygen-to-fuel ratio, the increase in temperature leads to significant decreases of the total tar yield, as seen in the case of LD slag at 860 and 920 °C. A higher oxygen-to-fuel ratio usually causes a lower tar yield and as seen in the cases of LD slag and iron sand. Among the three OCs, ilmenite has the highest tar production,

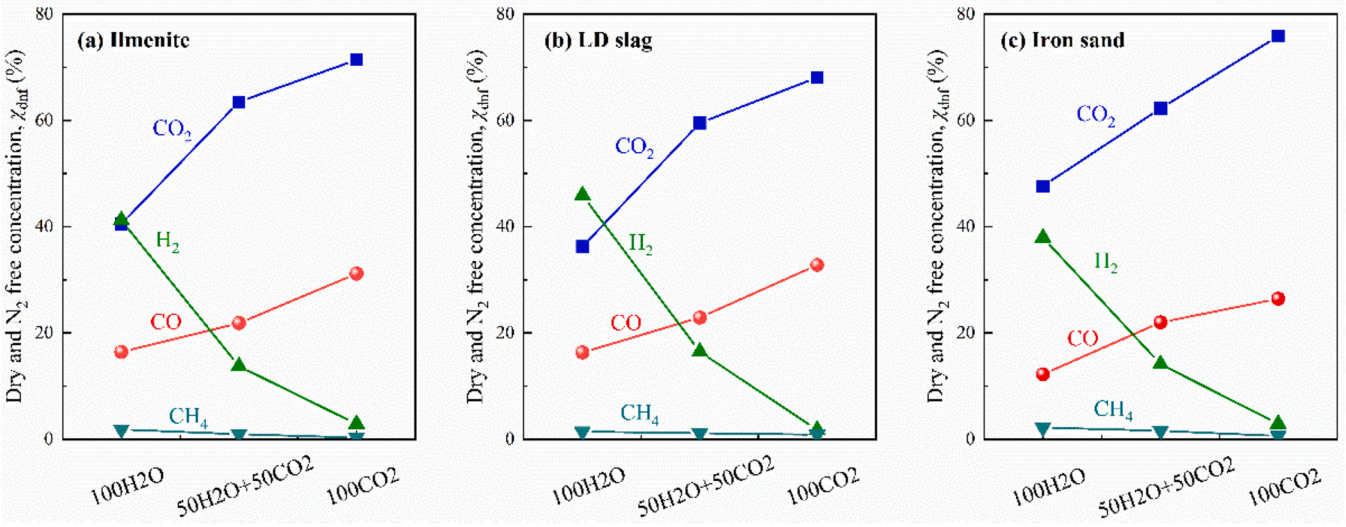


Fig. 9. Effect of gasification agent on the gas composition (dry and N_2 free basis), $\lambda \approx 0.3$, $T_{FR} = 920$ °C (except Test 19 and 20 whose temperature is 890 °C). Results are from Test 5, 6 and 7 for ilmenite, Test 9, 14 and 15 for LD slag and Test 16, 19 and 20 for iron sand.

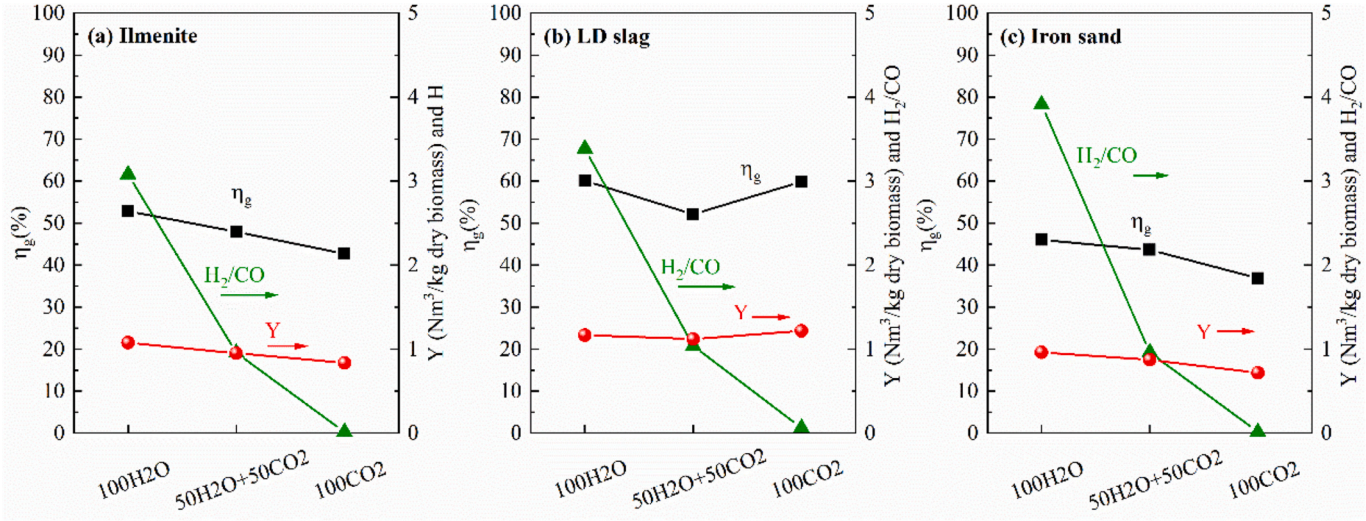


Fig. 10. Effect of gasification agent on Y, cold gas efficiency (η_g) and H_2/CO. Results are from Test 5, 6 and 7 for ilmenite, Test 9, 14 and 15 for LD slag and Test 16, 19 and 20 for iron sand with $\lambda \approx 0.3$ at $T_{FR} = 920$ °C (except Test 19 and 20 whose temperature is 890 °C).

while the LD slag has the lowest tar production. This can be mainly attributed to LD slag's high content of CaO and other Ca-based species which are typical catalysts for tar cracking [49,50]. These Ca species lower the activation energies for breaking critical bonds in aromatic rings and functional groups, like C_{ar}-C_{ar}, C_{ar}-OH and C_{ar}-COOH, and thus promote the decomposition of heavy aromatic hydrocarbons and facilitate their conversion to lighter gaseous products [51,52]. Calcium interaction with water also generates active hydrogen and hydroxyl radicals on the surface of Ca-containing compounds, and these radicals further enhance tar decomposition and steam reforming [44,53]. In addition, the porous/fluffy particle structure of LD slag may further facilitate gas-solid interactions, improving the contact between tar compounds and active sites. As a result, heavy aromatic species such as naphthalene are more effectively decomposed.

Fig. 12 presents the distribution of individual tar compounds. Naphthalene is identified as the dominant species, accounting for approximately 80–90% of the weight of the total tar amount. In the case of ilmenite, the naphthalene yield reached to around 1 g/kg dry microalgae, while the iron sand has a 0.7 g/kg naphthalene. LD slag has the lowest naphthalene yield at around 0.5 g/kg microalgae. In addition, benzene is detected with concentrations approaching 0.05 g/kg, and other species, including toluene, indene, and phenanthrene, are also present but in significantly lower amounts. The dominance of naphthalene suggests that most primary tars have undergone partial cracking and reforming that leaves relatively stable polycyclic aromatic hydrocarbons as the main residual species [54,55]. We have noticed that the high nitrogen content of microalgae may lead to formation of nitrogenous tar compounds, but we couldn't get information on these compounds because the GC–MS instrument doesn't have a column and was not calibrated for these compounds. Future studies could be put on identification and quantification of the nitrogen-containing tar compounds and their evolution during CLG operation.

Fig. 13 shows the NOx concentration from FR and fuel nitrogen conversion (X_{fn}) when using ilmenite under different operating conditions. The results indicate that NO is the dominant nitrogen-containing species, with concentrations of 10,600 ppm, while NO_2 and N_2O are present at significantly lower levels, typically around 100 ppm and 10 ppm, respectively. This distribution suggests that fuel-bound nitrogen in microalgae is primarily converted to NO under the investigated conditions, and the conversion to NO is around 14.1–17.2%, while the

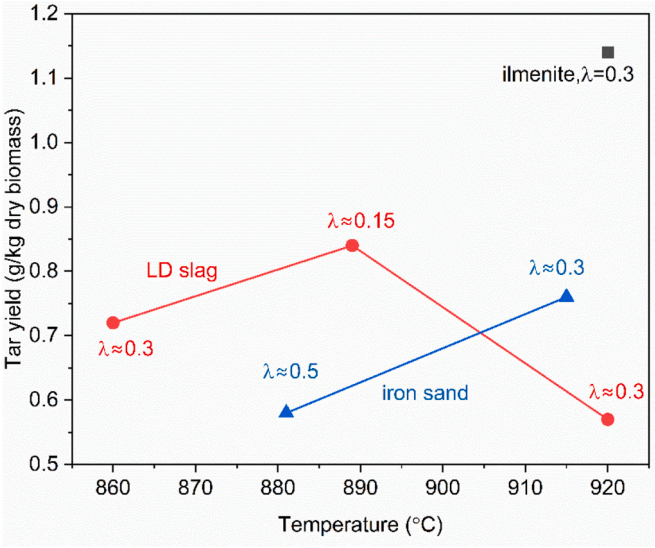


Fig. 11. Overall tar yield in typical campaigns with the three OCs. Data of ilmenite is from Test 5, LD slag is from Test 12 (λ ≈ 0.3 and 860 °C), Test 13 (λ ≈ 0.15 and 890 °C) and Test 9 (λ ≈ 0.3 and 920 °C), and iron sand is from Test 17 (λ ≈ 0.5 and 880 °C) and Test 16 (λ ≈ 0.3 and 920 °C).

conversion to NO_2 is below 0.3%. The FR temperature has little influence on the NOx formation, while the use of CO_2 replacing partly or fully the steam can lower the NO formation slightly. The weak dependence of NOx on the temperature and gasifying agents may be attributed to the fact that NO formation is largely governed by the release and subsequent oxidation of nitrogen-containing intermediates (e.g., NH_3 and HCN) during devolatilization and gasification, rather than by gas-phase temperature alone [56–59]. The NH_3 can react directly with the oxygen carrier through the reaction "$2NH_3 + 5Fe_2TiO_5 = 5FeTiO_3 + 5FeO + 2NO + 3H_2O$" while NO is generated and the Fe_2TiO_5 is reduced to $FeTiO_3$ and FeO [58,59]. The HCN follows similar mechanism of conversion and with NO, CO_2 and H_2O as gas products. In addition, the reducing environment in the FR when the oxygen carrier is well reduced the oxygen carrier compound (Fe_3O_4 or $FeTiO_3$) may also play a catalyzing role for homogeneous conversion of NO to N2 through "$2NO + 2NO_2 + 4NH_3 = 4N_2 + 6H_2O$". This may partially suppress the further oxidation of NO to NO_2, thereby maintaining NO as the predominant species.

4.3. Characterization of the OCs

The physicochemical properties of the OCs before and after the BCLG operation were investigated using ICP-OES, SEM-EDX, XRD and TGA analysis techniques. The aim is to explore the relationship between the materials' characteristics and the observed gasification performance and operational stability.

4.3.1. Morphology

The SEM–EDX results confirm clear compositional differences in the three OCs. Ilmenite is dominated by Fe and Ti, LD slag mainly consists of Ca and Fe with a noticeable Si contribution, whereas iron sand is primarily composed by Fe while having Si as the secondary element. Fig. 14 reveals distinct morphological evolutions of OC particles before and after BCLG operation. For ilmenite, the widely recognized core-shell structure is seen, and there is a significant change in structure of the samples before and after use with the microalgae. The ilmenite's core-shell structure is further discussed below, see Figs. 15 and 16. The particles exhibit rough surfaces and well-developed porous structures after operations, showing rich gas channels that can enhance the contact between gas and active sites in the OCs which finally may improve the overall reaction performance. Despite rich channels in and some cracks on the used ilmenite, the particles seem have a good integrity and no agglomeration is found, and thus facilitating the fluidization ability and experimental stability, as seen in Fig. 3 above. More cracks are found on and inside the LD slag particles and no agglomeration happens. A significant population of fine particles is observed surrounding large LD slag particles, whereas the fragmentation is much less pronounced for ilmenite and iron sand. And this can be a reason for the observed slightly higher fraction of elutriated particles in the cyclone in the campaign with LD slag. In contrast, the iron sand particles had relatively smooth and dense surfaces, which is a nature of the iron sand and would hinder gas diffusion and limit the reaction surface area during the reactions. The distinct particle morphologies and porous properties are in good

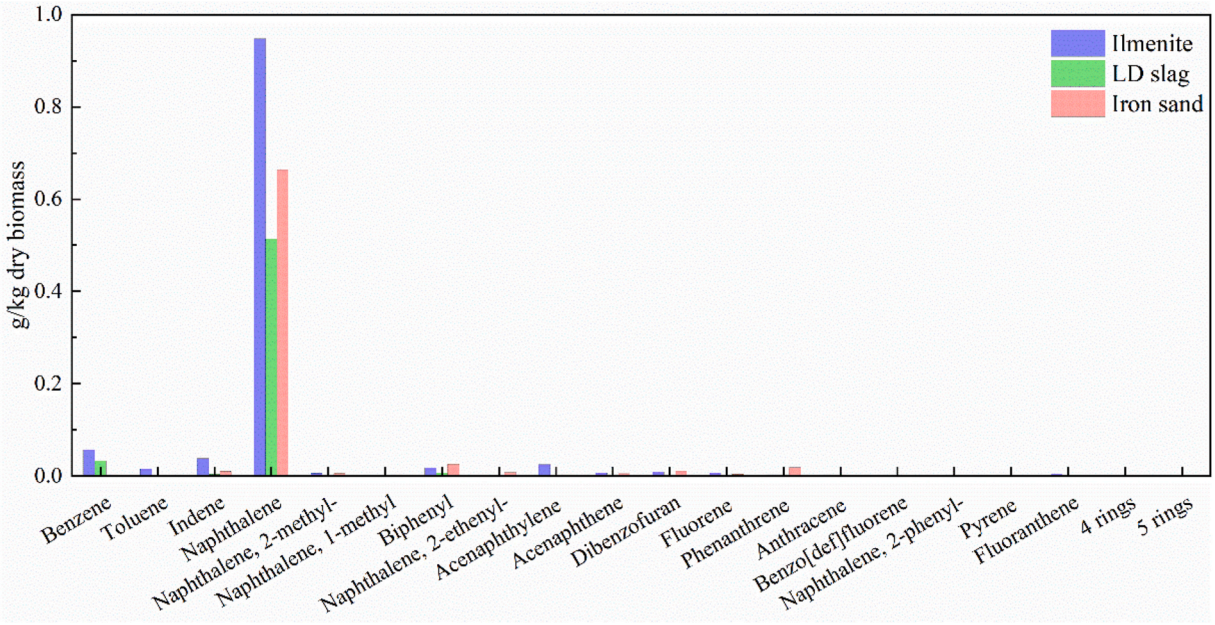


Fig. 12. Yield of tar compound in typical BCLG process with the ilmenite (Test 5), LD slag (Test 9) and iron sand (Test 16) in the gasification with 100% steam and oxygen-to-fuel ratio of around 0.3 at 920 °C.

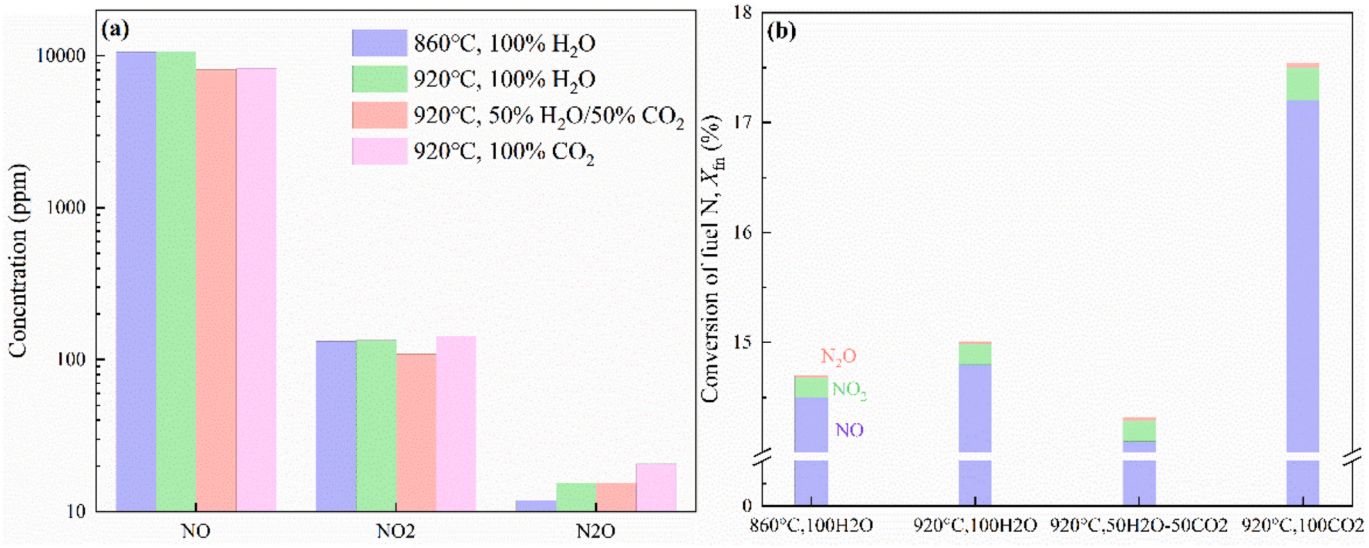


Fig. 13. (a) NO, NO_2 and N_2O concentrations at the FR exit and (b) conversion of fuel nitrogen to NO, NO_2 and N_2O under different operating conditions using ilmenite as the OC. Data for 860 °C and 100%H_2O is from Test 4, for 920 °C and 100%H_2O is from Test 5, for 920C and 50%H_2O/50%CO_2 is from Test 6 and for 920 °C and 100%CO_2 is from Test 7.

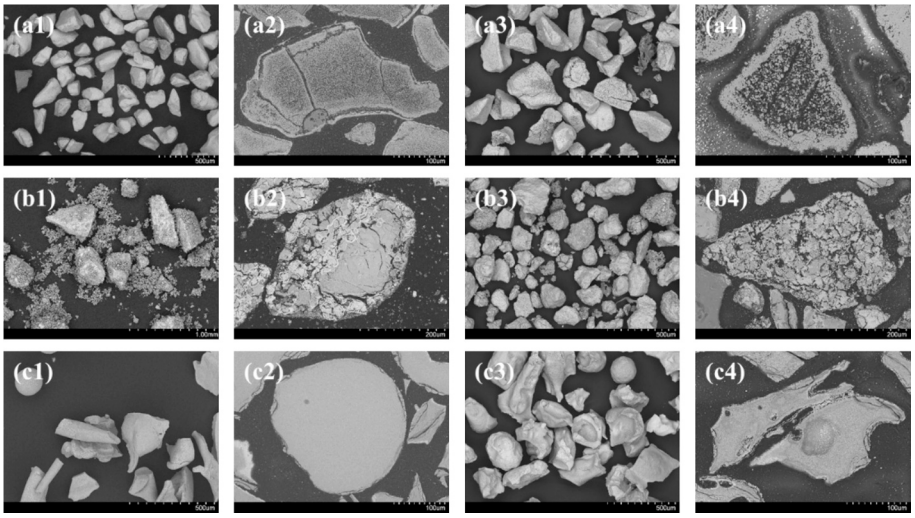


Fig. 14. SEM images of ilmenite (a1-a4), LD slag (b1-b4) and iron sand (c1-c4) before and after use in the 1.5 kW_{th} unit experiments, the images a2, a4, b2, b4, c2 and c4 are for cross-sections of the particles. For each OC, the first two SEM images (marked with 1 and 2) are before operation, and the last two images (marked with 3 and 4) are after operation.

agreement with the gasification performance observed in the pilot unit. The more porous ilmenite and LD slag enhance gas-solid contact and mass transfer, thus have shown better CLG performance than the denser surface iron sand, see Fig. 4 above as an example.

The core-shell structure of ilmenite is further analyzed with EDX techniques for several selected points adjacent to the particle surface, as seen in Fig. 15. Along the direction toward shell, the increase of iron (Fe) content (from 30.3 to 41.7 wt%) shows clearly that the iron migrated toward the surface of the particles, and this is consistent with the conclusions of previous studies regarding the application of ilmenite in a batch reactor [33] and in CLC process [60].

Fig. 16 shows the EDX elemental mapping of three single OC particles before and after the BCLG operation. We selected several elements that are abundant in the microalgae, along with the primary elements of the OCs, for analyses. It can be observed that after the use in BCLG, again the iron enriched on the shell, while potassium (K) tends to penetrate toward the core of the ilmenite particles (and few or no K accumulation in the shell). There is also some phosphorus (P) found in the OC particles, but this element is more uniformly distributed throughout the entire particles as compared to K. The migration of alkalis toward center of particles and iron toward the surface of particles (and later being worn out during circulations) can be linked with the ilmenite's lower reactivity after the campaign, as discussed in Section 4.3.3 below.

For LD slag, its porous and fluffy internal structure allows the original OC components, Ca, Si and Fe, to maintain relatively uniform across the particle. The AAEMs from microalgae ash have little penetration to the particle interior, thereby mitigating internal contamination and maintaining the overall original functionality of the OC.

For the iron sand particles, K and Ca have a much higher content in the particles after operation, specifically the K is more interior and Ca is more at the surface of particles. This indicates that AAEMs from the biomass undergo internal penetration within the OCs, while no significant changes in the distribution of Fe and Si elements were observed before and after the campaign.

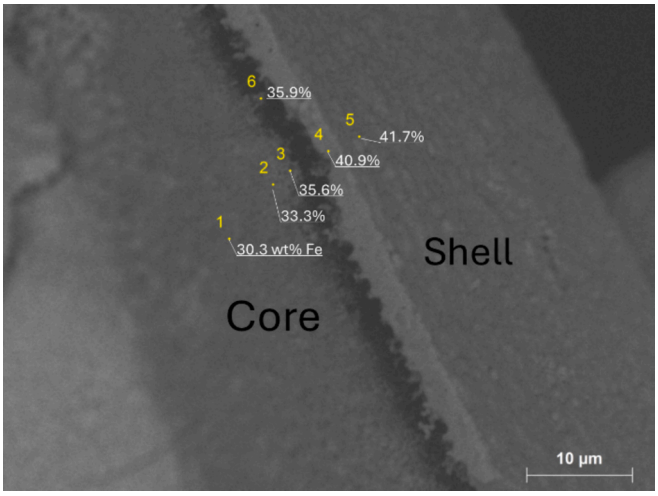


Fig. 15. Migration of iron element toward the surface of ilmenite, the points 1–3 are on the particle's core, points 4 and 5 are on the particle's shell and point 6 is at a similar front as point 3. The numbers in white color are the weight percentages of iron.

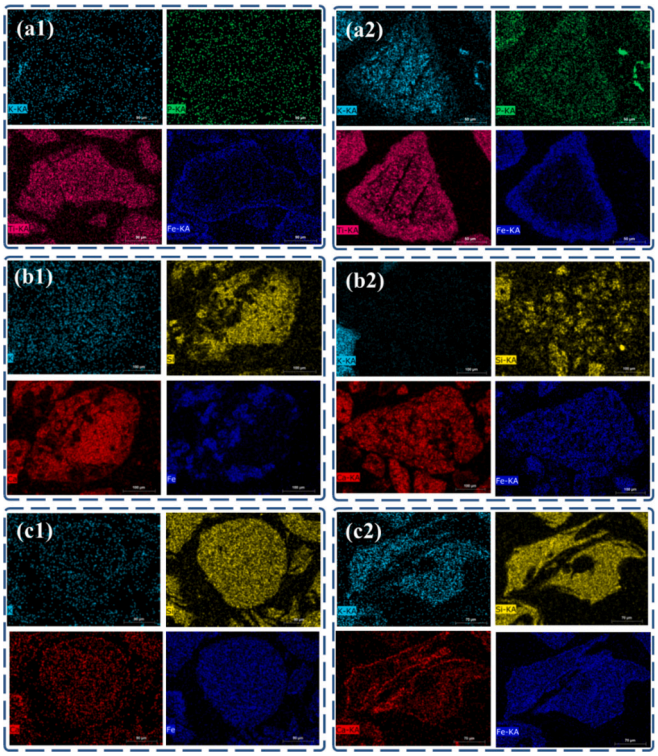


Fig. 16. EDX mapping of cross-sections of ilmenite (a1-a2), LD slag (b1-b2) and iron sand (c1-c2) before and after operating in the 1.5 kW_{th} unit experiments. The EDX images on the left are before operation and on the right are after operation.

For long-term operation, it can be seen that the clear alkali penetration and cumulation in the ilmenite may lead to decreases in oxygen transport, active sites amount and lower reactivities. In addition, the risk of agglomeration and defluidization may also rise as more alkalis are accumulated in the particles. These all are disadvantageous for the material's stabilities in reactivity and operationality. And this is less likely to happen to LD slag and iron sand that have less affinity to the alkalis in the microalgae.

Signs of ash-OC interaction and slight combination were observed in some LD slag and iron sand particles after the BCLG operation. But no signs of particles agglomeration and sintering were seen during all the campaign, and the bed fluidization went well. Fig. 17 presents the EDX line-scanning across representative cross-sections of LD slag and iron sand particles, illustrating the spatial distribution of major elements after operation.

For LD slag, two adjacent particles were seen with markedly different elemental distributions. The bigger particle on the left might be from the microalgae ash which shows primarily O and Na signals, with little other elements. Whereas the smaller particle on the right contains significant amounts of Ca, Fe, and Si and is a typical LD slag particle. This shows that the ash compound sodium (Na) can interact with the LD slag, especially with the sites where there is more calcium and silicon. It is clear in Fig. 17(a) that the LD slag particle (or fines) has a good contact with the microalgae ash, and this contact might happen at the beginning of gasification when the catalysis of Ca-based species in the LD slag was triggered.

For iron sand, see Fig. 17(b), a clear enrichment of Fe is observed at the interface between two particles, accompanied by a decrease in oxygen content, thus there is an increase in the Fe/O ratio. This phenomenon suggests localized combination and possible partial reduction at particles' contact points, which may promote inter-particle bonding. Within the bulk of the particles, however, Fe and Si remain relatively uniform, with an approximate Fe:Si ratio of 1:2, indicating that the primary mineral composition of iron sand is largely preserved during operation.

4.3.2. *Crystalline phase*

Fig. 18 compares the XRD patterns of the three OCs before and after the campaigns. It is noted that the ilmenite in this study had already been used in prior chemical looping gasification tests with waste wood and can therefore be considered in activated state. Its crystalline phases before and after the microalgae campaign are mainly TiO_2, Fe_3O_4, and Fe_2TiO_5, indicating a relatively stable phase composition. After use with microalgae, no new crystalline phases are detected by XRD; however, potassium incorporation into the ilmenite particles is evidenced by the SEM–EDX results as seen in Fig. 16 above. This suggests that alkali species from microalgae ash are likely present in amorphous form or at concentrations below the limit of XRD detection, while still interacting with the OC. Similar alkali–ilmenite interactions have also been reported in larger scale units, confirming a strong affinity between biomass-derived alkali metals and iron-titanium phases [27,61].

LD slag and iron sand were not used in any prior experiments and were only used in the present experiments. After CLG operation, the XRD patterns of these two OCs have no significant phase changes, indicating that their bulk crystalline structures remain largely stable during the campaign. However, it is observed that the intensities of MgO in LD slag and Fe_3O_4 in iron sand are stronger in the fresh samples and decrease slightly after operation. The magnesium is from the LD process where MgO is added to protect the wall of the process's high-temperature furnace. This decrease of peak intensity may indicate a decrease in crystallinity or partial structural reordering induced by repeated redox cycling and interaction with biomass-derived ash. In addition, the deposition of ash species on particle surfaces may decrease the diffraction signals. Despite these changes, the absence of new crystalline phases suggests that phase transformation is limited under the investigated conditions, likely due to the relatively short operating time and insufficient extent of solid-solid interactions. The good phase stability of the OCs ensures stable particle properties and thus stable fluid dynamics properties in the fluidization system, and this makes a good basis for the continuous campaigns which could last for dozens of hours.

4.3.3. *Reactivity of the oxygen carriers*

The materials reactivity was measured with redox experiments in TGA at 950 °C with a 15 vol% $H_2 + N_2$ mixture as reducing gas and air as oxidizing gas. Fig. 19 (a, b and c) compares the material conversion over

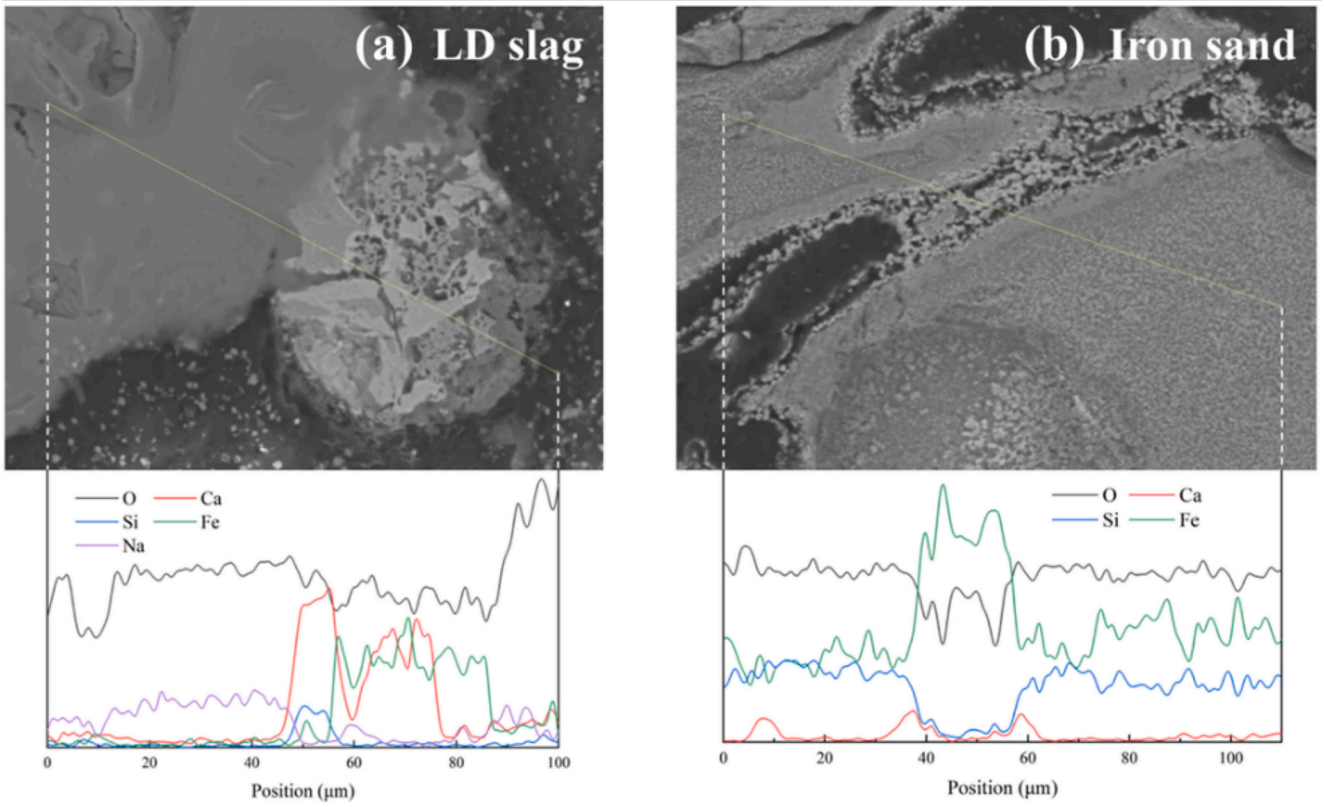


Fig. 17. EDX line-scanning analysis of the cross-sections of (a) LD slag and (b) iron sand particles after the continuous CLG campaign with the microalgae.

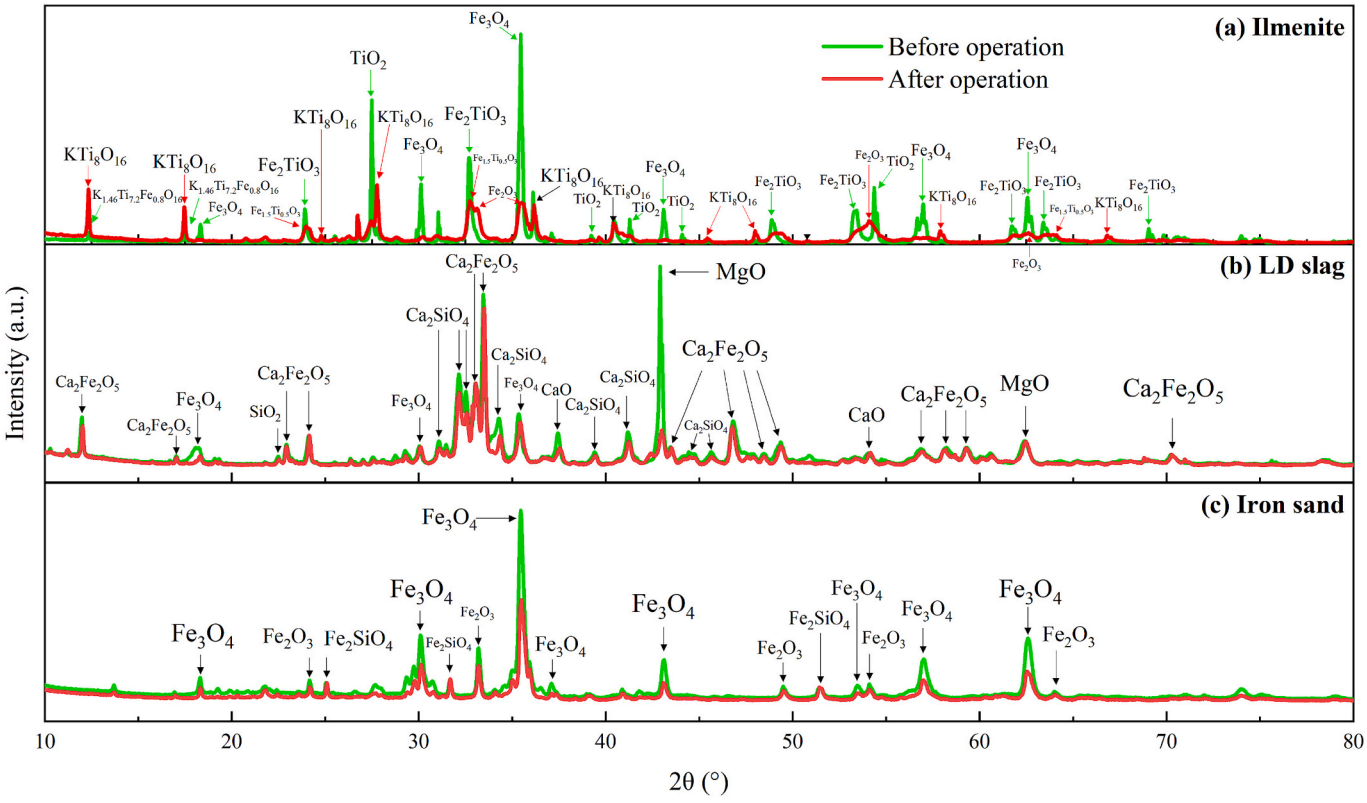


Fig. 18. XRD phases in the OCs before (in green color) and after (in red color) the BCLG campaign. Phases that remain unchanged before and after use are marked with black arrows, while some unique phases are marked with the same color as their corresponding original patterns (green color is for samples before the campaign and red color for samples after the campaign).

time during reduction with H_2 for the OCs before and after the campaigns. After use in the BCLG campaign, the ilmenite needs a longer time to reduce, indicating a lower reduction activity. This can be attributed to the interaction between biomass-derived alkali metals (e.g., K and Na) and the active iron-based phases, as seen above in Fig. 16. The interaction may alter the oxygen transfer properties, thereby lowering the reduction kinetics. In the meantime, the outward migration of iron species, which leads to formation of a Fe-rich layer, may also result in gradual attrition of this active surface during prolonged operation. The loss of this iron-enriched layer reduces the availability of reactive sites and in the end leads to a lower oxygen transfer capacity. As compared to ilmenite, the LD slag and iron sand reactivities are more stable during the pilot experiments, and this suggests that their active phases are less affected by alkali interactions and mechanical attrition. The $(rate\ index)_{TGA}$ with H_2 reduction is summarized in Table 7 to quantify the reactivity of the three OCs before and after operation. It can be observed clearly that the reactivity of ilmenite decreases significantly after operation, which is consistent with the longer reduction time required for the used sample. In contrast, LD slag and iron sand show only minor differences in the rate index before and after use, indicating that their reactivity remains relatively stable during the CLG process.

The oxidation behavior of the OCs was also studied with reaction profiles obtained from TGA, as shown in Fig. 19 (d, e and f). The reactivity of ilmenite and LD slag kept quite similar before and after the campaigns. The iron sand oxidation reactivity went down a bit after use in the campaign, and this can be attributed to partial surface modification, such as the deposition of ash species or slight structural changes during redoxes, which can hinder oxygen diffusion to some extent.

5. Discussion

In the pre-activation and the current microalgae campaign, the ilmenite always shows good flowability, stable fluidizations and satisfying activity and operationality. This confirms ilmenite's position of benchmark material in the chemical looping area. LD slag, although not a benchmark material, has shown stable fluidization, excellent operationality and higher reactivity as compared to ilmenite. What's more interesting and exciting is its catalytic activity over the gasification and tar cracking. This catalysis effect could last long and probably can function through the whole life of the LD slag particles, because the calcium oxide (catalyst to gasification) stays well in the bulk of the LD slag and seems not tends to leave (e.g., through abrasion) the bulk particles during the campaign. So, a long-time catalysis and thus fast gasification can be expected with this material. In addition, LD slag is a waste from industry, abundant and cheap, and thus less capital cost of the CLG system is foreseeable. Iron sand is although another industrial waste, it is however much less abundant than LD slag and much harder to handle in the 1.5 kW fluidization system than LD slag and ilmenite.

Table 7
Rate index (%/min) of the three OCs calculated from the reactivity rests in TGA with 15% H_2 at 950 °C.

	Before operation	After operation
Ilmenite	8.5	2.4
LD slag	6.7	6.1
Iron sand	5.3	5.6

The raw syngas quality from the ilmenite and LD slag campaigns are much better than the iron sand campaign, and there are more CO_2 from the iron sand process left behind for downstream processing. This will very likely improve the costs for downstream CO_2 separation, capture, reutilization and other processing.

While LD slag shows better performances over ilmenite and iron sand in many aspects, this material exhibited less particle integrity that may be a signal of a higher attrition and shorter lifetime, but this needs more and longer time tests in CLG conditions.

6. Conclusions

LD slag is the most operatable material among the three oxygen carriers (ilmenite, LD slag and iron sand) during the campaigns. As compared with ilmenite and iron sand, LD slag shows a more favorable

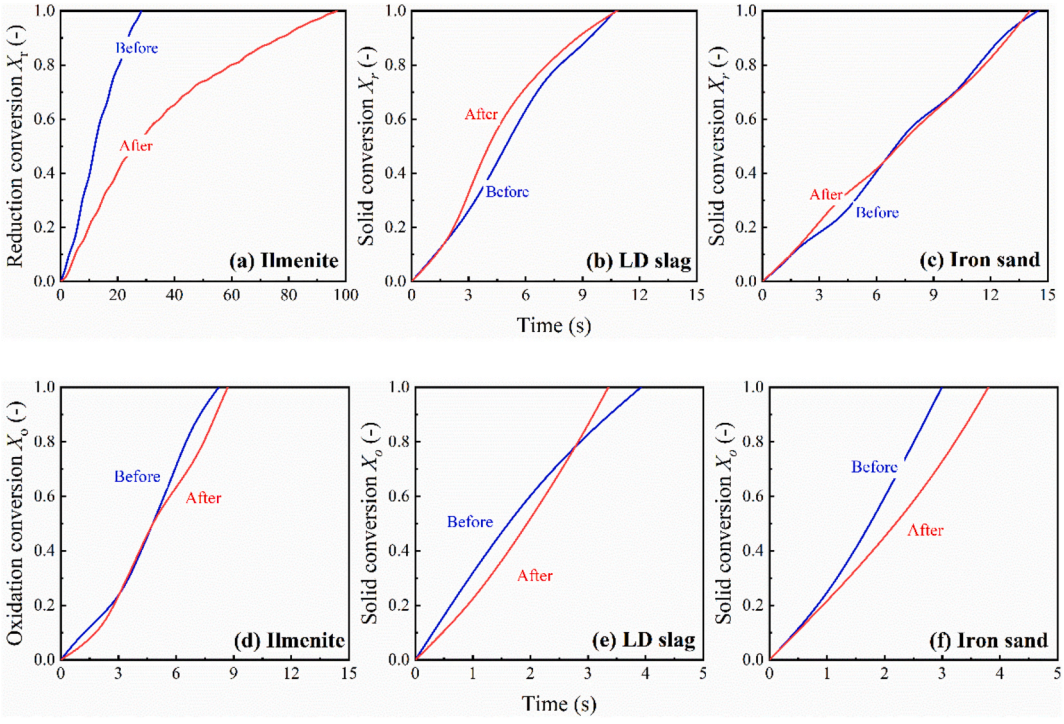


Fig. 19. Conversion of the ilmenite (a, d), LD slag (b, e) and iron sand (c, f) in the reduction with 15% H_2 (a, b, c) and in the oxidation with air (d, e, f) at 950 °C. Curves in blue color are of the oxygen carriers before the campaign and in red color are after the campaign.

balance between material reactivity, stability, and syngas quality. Although all three OCs achieve a high biomass conversion and a low carbon emission from the AR, the LD slag has the fastest gasification, highest syngas yield (1.5 Nm^3/kg microalgae), highest microalgae conversion (~100%) and highest cold gas efficiency (65%). In addition, the LD slag has a low tar yield, particularly for heavier aromatic compounds. The LD slag has a tar yield of around 0.5 g/kg microalgae and this is around half of that with ilmenite and iron sand, and the main tar compound are all naphthalene which takes of around 80–90% of the total tar amount. For the ilmenite, the usually observed potassium and sodium penetration is also seen in the current work, while this is not seen when using LD slag and iron sand, could be a result of shorter operation time.

The outstanding performance of LD slag in the microalgae CLG process indicates a more effective conversion of intermediates and improved syngas quality, and this is likely related to LD slag's Ca-rich composition, which is a catalyst and can promote gasification and tar cracking reactions.

CRediT authorship contribution statement

Hantao Lu: Writing – review & editing, Writing – original draft, Visualization, Methodology, Investigation, Formal analysis, Data curation. **Daofeng Mei:** Writing – review & editing, Visualization, Supervision, Resources, Project administration, Investigation, Funding acquisition, Formal analysis, Data curation, Conceptualization. **Francisco García-Labiano:** Writing – review & editing, Supervision, Resources, Project administration, Methodology, Investigation, Funding acquisition, Conceptualization. **Juan Ignacio Ruiz Irizar:** Resources, Methodology, Investigation. **Maria Teresa Izquierdo:** Writing – review & editing, Resources, Methodology, Investigation, Formal analysis. **Alberto Abad:** Writing – review & editing, Supervision, Resources, Methodology, Conceptualization. **Guangsuo Yu:** Writing – review & editing, Supervision, Resources, Funding acquisition.

Declaration of competing interest

The authors declare that they have no known competing financial interests or personal relationships that could have appeared to influence the work reported in this paper.

Acknowledgement

This research was funded by the "CLG-G3BioF" project that received funding from the Horizon Europe Framework Programme under Marie Sklodowska-Curie grant agreement (No. 101110366) and by the "Bio-MeGaFuel" project from the Horizon Europe (No. 101147737). Hantao Lu thanks the China Scholarship Council for providing the scholarship (No. 202406740039).

Data availability

Data will be made available on request.

References

[1] A. AlNouss, G. McKay, T. Al-Ansari, Production of syngas via gasification using optimum blends of biomass, J. Clean. Prod. 242 (2020) 118499, https://doi.org/10.1016/j.jclepro.2019.118499.
[2] H. Lu, Y. Gong, C. Areeprasert, L. Ding, Q. Guo, W.-H. Chen, G. Yu, Integration of biomass torrefaction and gasification based on biomass classification: a review, Energ. Technol. 9 (2021) 2001108, https://doi.org/10.1002/ente.202001108.
[3] A. Larsson, M. Kuba, T. Berdugo Vilches, M. Seemann, H. Hofbauer, H. Thunman, Steam gasification of biomass – typical gas quality and operational strategies derived from industrial-scale plants, Fuel Process. Technol. 212 (2021) 106609, https://doi.org/10.1016/j.fuproc.2020.106609.
[4] V.S. Sikarwar, M. Zhao, P.S. Fennell, N. Shah, E.J. Anthony, Progress in biofuel production from gasification, Prog. Energy Combust. Sci. 61 (2017) 189–248, https://doi.org/10.1016/j.pecs.2017.04.001.
[5] S. HUSEYIN, G. WEI, H. LI, F. HE, Z. HUANG, Chemical-looping gasification of biomass in a 10 kWth interconnected fluidized bed reactor using Fe_2O_3/Al_2O_3 oxygen carrier, J. Fuel Chem. Technol. 42 (2014) 922–931, https://doi.org/10.1016/S1872-5813(14)60039-6.
[6] Y. Li, B. Zhang, X. Yang, B. Yang, S. Zhang, Z. Wu, Chemical looping reforming of the micromolecular component from biomass pyrolysis via Fe_2O_3@SBA-16, Int. J. Coal Sci. Technol. 11 (2024) 35, https://doi.org/10.1007/s40789-024-00691-z.
[7] J. Adánez, A. Abad, T. Mendiara, P. Gayán, L.F. de Diego, F. García-Labiano, Chemical looping combustion of solid fuels, Prog. Energy Combust. Sci. 65 (2018) 6–66, https://doi.org/10.1016/j.pecs.2017.07.005.
[8] P. Dieringer, F. Marx, F. Alobaid, J. Ströhle, B. Epple, Process control strategies in chemical looping gasification—a novel process for the production of biofuels allowing for net negative CO2 emissions, Appl. Sci. 10 (2020) 4271, https://doi.org/10.3390/app10124271.
[9] T. Mattison, F. Hildor, Y. Li, C. Linderholm, Negative emissions of carbon dioxide through chemical-looping combustion (CLC) and gasification (CLG) using oxygen carriers based on manganese and iron, Mitig. Adapt. Strateg. Glob. Chang. 25 (2020) 497–517, https://doi.org/10.1007/s11027-019-09860-x.
[10] X. Zhao, H. Zhou, V.S. Sikarwar, M. Zhao, A.-H.A. Park, P.S. Fennell, L. Shen, L.-S. Fan, Biomass-based chemical looping technologies: the good, the bad and the future, Energy Environ. Sci. 10 (2017) 1885–1910, https://doi.org/10.1039/C6EE03718F.
[11] A. Di Giuliano, S. Capone, M. Anatone, K. Gallucci, Chemical looping combustion and gasification: a review and a focus on European research projects, Ind. Eng. Chem. Res. 61 (2022) 14403–14432, https://doi.org/10.1021/acs.iecr.2c02677.
[12] R.A. Lee, J.-M. Lavoie, From first- to third-generation biofuels: challenges of producing a commodity from a biomass of increasing complexity, Anim. Front. 3 (2013) 6–11, https://doi.org/10.2527/af.2013-0010.
[13] Y. Chisti, Biodiesel from microalgae, Biotechnol. Adv. 25 (2007) 294–306, https://doi.org/10.1016/j.biotechadv.2007.02.001.
[14] L. Laurens, State of Technology Review - Algae Bioenergy, 2017, https://doi.org/10.13140/RG.2.2.11770.90560.
[15] T. Sathish, R. Saravanan, J. Giri, A.A.A. l-Kahtani, C. Prakash, A. Kumar, V. J. Angadi, S. Wang, M. Ubaidullah, Hydrogen conversion by microalgae through water gasification under different operating conditions, and Fe_2O_3, Al_2O_3, and CaO additives: an experimental study, Int. J. Hydrog. Energy 104 (2025) 289–301, https://doi.org/10.1016/j.ijhydene.2024.09.003.
[16] K. Heeley, R.L. Orozco, Z. Shah, L.E. Macaskie, J. Love, B. Al-Duri, Supercritical water gasification of microalgae: the impact of the algal growth water, J. Supercrit. Fluids 205 (2024) 106143, https://doi.org/10.1016/j.supflu.2023.106143.
[17] Z. Sun, S. Cao, A.Y. Ugya, S.N. Agathos, L. Sun, J. Li, Research advances in gasification process modelling for syngas production from microalgal biomass, Fuel 416 (2026) 138543, https://doi.org/10.1016/j.fuel.2026.138543.
[18] Y. Liu, K. Yin, J. Wu, D. Mei, J. Konttinen, T. Joronen, Z. Hu, C. He, Ash chemistry in chemical looping process for biomass valorization: a review, Chem. Eng. J. 478 (2023) 147429, https://doi.org/10.1016/j.cej.2023.147429.
[19] F. Störner, F. Hildor, H. Leion, M. Zevenhoven, L. Hupa, M. Rydén, Potassium ash interactions with oxygen carriers steel converter slag and Iron mill scale in chemical-looping combustion of biomass—experimental evaluation using model compounds, Energy Fuel 34 (2020) 2304–2314, https://doi.org/10.1021/acs.energyfuels.9b03616.
[20] G. Liu, Y. Liao, Y. Wu, X. Ma, L. Chen, Characteristics of microalgae gasification through chemical looping in the presence of steam, Int. J. Hydrog. Energy 42 (2017) 22730–22742, https://doi.org/10.1016/j.ijhydene.2017.07.173.
[21] Y. Liu, T. Wang, X. Zhang, X. Hu, T. Liu, Q. Guo, Chemical looping staged conversion of microalgae with calcium ferrite as oxygen carrier: pyrolysis and gasification characteristics, J. Anal. Appl. Pyrolysis 156 (2021) 105129, https://doi.org/10.1016/j.jaap.2021.105129.
[22] G. Liu, Y. Liao, Y. Wu, X. Ma, Evaluation of Sr-substituted Ca2Fe2O5 as oxygen carrier in microalgae chemical looping gasification, Fuel Process. Technol. 191 (2019) 93–103, https://doi.org/10.1016/j.fuproc.2019.03.019.
[23] M. Rydén, M. Hanning, F. Lind, Oxygen carrier aided combustion (OCAC) of wood chips in a 12 MWth circulating fluidized bed boiler using steel converter slag as bed material, Appl. Sci. 8 (2018) 2657, https://doi.org/10.3390/app8122657.
[24] M. Rydén, M. Hanning, A. Corcoran, F. Lind, Oxygen carrier aided combustion (OCAC) of wood chips in a semi-commercial circulating fluidized bed boiler using manganese ore as bed material, Appl. Sci. 6 (2016) 347, https://doi.org/10.3390/app6110347.
[25] H. Leion, A. Lyngfelt, M. Johansson, E. Jerndal, T. Mattisson, The use of ilmenite as an oxygen carrier in chemical-looping combustion, Chem. Eng. Res. Des. 86 (2008) 1017–1026, https://doi.org/10.1016/j.cherd.2008.03.019.
[26] A. Lyngfelt, D. Pallarès, C. Linderholm, F. Lind, H. Thunman, B. Leckner, Achieving adequate circulation in chemical looping combustion—design proposal for a 200 MWth chemical looping combustion circulating fluidized bed boiler, Energy Fuel 36 (2022) 9588–9615, https://doi.org/10.1021/acs.energyfuels.1c03615.
[27] O. Condori, A. Abad, M.T. Izquierdo, L.F. de Diego, F. García-Labiano, J. Adánez, Assessment of the chemical looping gasification of wheat straw pellets at the 20 kWth scale, Fuel 344 (2023) 128059, https://doi.org/10.1016/j.fuel.2023.128059.
[28] O. Condori, F. García-Labiano, L.F. de Diego, M.T. Izquierdo, A. Abad, J. Adánez, Biomass chemical looping gasification for syngas production using LD slag as oxygen carrier in a 1.5 kWth unit, Fuel Process. Technol. 222 (2021) 106963, https://doi.org/10.1016/j.fuproc.2021.106963.
[29] F. Hildor, A.H. Soleimanisalim, M. Seemann, T. Mattisson, H. Leion, Tar characteristics generated from a 10 kWth chemical-looping biomass gasifier using steel converter slag as an oxygen carrier, Fuel 331 (2023) 125770, https://doi.org/10.1016/j.fuel.2022.125770.

[30] V. Purnomo, I. Staničić, D. Mei, A.H. Soleimanisalim, T. Mattisson, M. Rydén, H. Leion, Performance of iron sand as an oxygen carrier at high reduction degrees and its potential use for chemical looping gasification, Fuel 339 (2023) 127310, https://doi.org/10.1016/j.fuel.2022.127310.
[31] Y. Lin, H. Wang, Y. Wang, R. Huo, Z. Huang, M. Liu, G. Wei, Z. Zhao, H. Li, Y. Fang, Review of biomass chemical looping gasification in China, Energy Fuel 34 (2020) 7847–7862, https://doi.org/10.1021/acs.energyfuels.0c01022.
[32] X. Liu, Q. Guo, Y. Qin, G. Wei, Y. Du, H. Liang, C. Miao, Y. Wei, C. He, Y. Yao, S. V. Vassilev, Chemical looping co-upgrading of vinegar residue and LD slag into syngas: insights into reduction kinetics mechanism and multi-cycle performance, J. Environ. Chem. Eng. 13 (2025) 116878, https://doi.org/10.1016/j.jece.2025.116878.
[33] D. Mei, F. García-Labiano, A. Abad, I. Adánez-Rubio, T. Mattisson, Evaluation of ilmenite, manganese ore, LD slag and iron sand oxygen carriers for chemical looping gasification with microalgae, Fuel Process. Technol. 275 (2025) 108266, https://doi.org/10.1016/j.fuproc.2025.108266.
[34] D. Mei, T. Mendiara, A. Abad, L.F. de Diego, F. García-Labiano, P. Gayán, J. Adánez, H. Zhao, Evaluation of manganese minerals for chemical looping combustion, Energy Fuel 29 (2015) 6605–6615, https://doi.org/10.1021/acs.energyfuels.5b01293.
[35] E. HRN, 18122: 2022; Solid Biofuels–Determination of Ash Content (ISO 18122: 2022; EN ISO 18122: 2022), Zagreb, Croatia, Croatian Standard Institute, 2022.
[36] O. Condori, L.F. de Diego, F. Garcia-Labiano, M.T. Izquierdo, A. Abad, J. Adánez, Syngas production in a 1.5 kWth biomass chemical looping gasification unit using Fe and Mn ores as the oxygen carrier, Energy Fuel 35 (2021) 17182–17196, https://doi.org/10.1021/acs.energyfuels.1c01878.
[37] P. Simell, P. Ståhlberg, E. Kurkela, J. Albrecht, S. Deutsch, K. Sjöström, Provisional protocol for the sampling and anlaysis of tar and particulates in the gas from large-scale biomass gasifiers. Version 1998, Biomass Bioenergy 18 (2000) 19–38, https://doi.org/10.1016/S0961-9534(99)00064-1.
[38] M. Sun, D. Zhang, Q. Yao, Y. Liu, X. Su, C.Q. Jia, Q. Hao, X. Ma, Separation and composition analysis of GC/MS analyzable and unanalyzable parts from coal tar, Energy Fuel 32 (2018) 7404–7411, https://doi.org/10.1021/acs.energyfuels.8b01054.
[39] A. Pérez-Astray, I. Adánez-Rubio, T. Mendiara, M.T. Izquierdo, A. Abad, P. Gayán, L.F. de Diego, F. García-Labiano, J. Adánez, Comparative study of fuel-N and tar evolution in chemical looping combustion of biomass under both iG-CLC and CLOU modes, Fuel 236 (2019) 598–607, https://doi.org/10.1016/j.fuel.2018.09.003.
[40] M. Johansson, T. Mattisson, A. Lyngfelt, Investigation of Fe2O3 with MgAl2O4 for chemical-looping combustion, Ind. Eng. Chem. Res. 43 (2004) 6978–6987, https://doi.org/10.1021/ie049813c.
[41] O. Condori, F. García-Labiano, L.F. de Diego, M.T. Izquierdo, A. Abad, J. Adánez, Biomass chemical looping gasification for syngas production using ilmenite as oxygen carrier in a 1.5 kWth unit, Chem. Eng. J. 405 (2021) 126679, https://doi.org/10.1016/j.cej.2020.126679.
[42] A. Lillebø, E. Rytter, E.A. Blekkan, A. Holmen, Fischer–Tropsch synthesis at high conversions on Al_2O_3-supported Co catalysts with different H_2/CO levels, Ind. Eng. Chem. Res. 56 (2017) 13281–13286, https://doi.org/10.1021/acs.iecr.7b01801.
[43] D. Mei, F. García-Labiano, A. Abad, T. Mattisson, Chemical looping gasification with microalgae: intrinsic gasification kinetics of char derived from fast pyrolysis, Energies 19 (2026) 276, https://doi.org/10.3390/en19010276.
[44] L. Liu, X. Zhou, Q. Liu, H. Zhou, N. Li, Y. Ban, Reaction path analysis of calcium-catalyzed steam gasification of lignite char and formation mechanism of hydrogen-rich syngas, Int. J. Hydrog. Energy 198 (2026) 152776, https://doi.org/10.1016/j.ijhydene.2025.152776.
[45] I.P. Lazzarotto, S.D. Ferreira, J. Junges, G.R. Bassanesi, C. Manera, D. Perondi, M. Godinho, The role of CaO in the steam gasification of plastic wastes recovered from the municipal solid waste in a fluidized bed reactor, Process. Saf. Environ. Prot. 140 (2020) 60–67, https://doi.org/10.1016/j.psep.2020.04.009.
[46] C. Zhou, T. Stuermer, R. Gunarathne, W. Yang, W. Blasiak, Effect of calcium oxide on high-temperature steam gasification of municipal solid waste, Fuel 122 (2014) 36–46, https://doi.org/10.1016/j.fuel.2014.01.029.
[47] B. Li, L. Wei, H. Yang, X. Wang, H. Chen, The enhancing mechanism of calcium oxide on water gas shift reaction for hydrogen production, Energy 68 (2014) 248–254, https://doi.org/10.1016/j.energy.2014.02.088.
[48] V. Purnomo, D. Mei, I. Staničić, T. Mattisson, H. Leion, Effect of the conversion degree on the apparent kinetics of Iron-based oxygen carriers, Energy Fuel 38 (13) (2024) 11824–11836, https://doi.org/10.1021/acs.energyfuels.4c00928.
[49] J. Yongbin, H. Jiejie, W. Yang, Effects of calcium oxide on the cracking of coal tar in the freeboard of a fluidized bed, Energy Fuel 18 (2004) 1625–1632, https://doi.org/10.1021/ef034077v.
[50] L. Zou, L. Ma, G. Wei, S. Deng, Q. Zhao, Catalytic tar cracking over calcium oxide-based bifunctional materials during biomass chemical looping gasification: experimental and DFT approaches, Fuel 418 (2026) 138736, https://doi.org/10.1016/j.fuel.2026.138736.
[51] X. Lin, C. Li, X. He, J. Dai, D. Xu, Y. Wang, Study on the mechanism of calcium catalyzed CO_2 gasification of lignite, Fuel Process. Technol. 213 (2021) 106689, https://doi.org/10.1016/j.fuproc.2020.106689.
[52] Y. Ban, Y. Wang, N. Li, R. He, K. Zhi, Q. Liu, The catalytic effect of calcium and potassium on CO_2 gasification of Shengli lignite: the role of carboxyl, Royal Society Open Science: Chemistry 5 (9) (2018) 180717, https://doi.org/10.1098/rsos.180717.
[53] Q. Luo, L. Zhang, Y. Bai, G. Lu, P. Lv, J. Wei, X. Song, J. Wang, W. Su, G. Yu, Insights into the catalytic mechanism of calcium species during char-H_2O/CO_2 gasification based on molecular reaction dynamics, J. Energy Inst. 117 (2024) 101831, https://doi.org/10.1016/j.joei.2024.101831.
[54] B. Wang, L. Wei, Y. Li, T. Yang, Y. Li, Q. Gan, Ca-catalysis mechanisms from coal pyrolysis to high energy density fuel precursors: multiscale insights via ReaxFF MD and experiment, J. Anal. Appl. Pyrolysis 192 (2025) 107305, https://doi.org/10.1016/j.jaap.2025.107305.
[55] K. Norinaga, H. Yang, R. Tanaka, S. Appari, K. Iwanaga, Y. Takashima, S. Kudo, T. Shoji, J. Hayashi, A mechanistic study on the reaction pathways leading to benzene and naphthalene in cellulose vapor phase cracking, Biomass Bioenergy 69 (2014) 144–154, https://doi.org/10.1016/j.biombioe.2014.07.008.
[56] D. Mei, A. Lyngfelt, T. Mattisson, C. Linderholm, Oxy-polishing of gas from chemical looping combustion: fuel-nitrogen transformation and model-aided gas purity optimization, Chem. Eng. J. 509 (2025) 161267, https://doi.org/10.1016/j.cej.2025.161267.
[57] D. Mei, C. Linderholm, A. Lyngfelt, Performance of an oxy-polishing step in the 100 kWth chemical looping combustion prototype, Chem. Eng. J. 409 (2021) 128202, https://doi.org/10.1016/j.cej.2020.128202.
[58] M. Cheng, F. Normann, D. Zhao, Z. Li, N. Cai, H. Leion, Oxidation of Ammonia by ilmenite under conditions relevant to chemical-looping combustion, Energy Fuel 29 (12) (2015) 8126–8134, https://doi.org/10.1021/acs.energyfuels.5b01939.
[59] L. Li, G. Sun, D. Lu, H. Liu, C. Liu, B. Jin, L. Duan, Volatile-N behavior in oxygen carrier aided solid waste combustion using a two-stage fluidized bed reactor, Energy Fuel 38 (21) (2024) 21322–21332, https://doi.org/10.1021/acs.energyfuels.4c02598.
[60] A. Cuadrat, A. Abad, J. Adánez, L.F. de Diego, F. García-Labiano, P. Gayán, Behavior of ilmenite as oxygen carrier in chemical-looping combustion, Fuel Process. Technol. 94 (2012) 101–112, https://doi.org/10.1016/j.fuproc.2011.10.020.
[61] O. Condori, A. Abad, F. García-Labiano, L.F. de Diego, MaríaT. Izquierdo, J. Adánez, Parametric evaluation of clean syngas production from pine forest residue by chemical looping gasification at the 20 kW_{th} scale, J. Clean. Prod. 436 (2024) 140434, https://doi.org/10.1016/j.jclepro.2023.140434.